Switchable resonant hyperpolarization transfer from phosphorus-31 nuclei to silicon-29 nuclei in natural silicon

by

Phillip Dluhy

B.Sc., Loyola University Chicago, 2012

Thesis Submitted in Partial Fulfillment
of the Requirements for the Degree of
Master of Science

in the
Department of Physics
Faculty of Science

SIMON FRASER UNIVERSITY
Summer 2015

Approval

Name:	Phillip Dluhy
Degree:	Master of Science (Physics)
Title:	*Switchable resonant hyperpolarization transfer from phosphorus-31 nuclei to silicon-29 nuclei in natural silicon*
Examining Committee:	**Chair:** Dr. Malcolm Kennett Associate Professor

Dr. Michael L. W. Thewalt
Senior Supervisor
Professor

Dr. David Broun
Supervisor
Associate Professor

Dr. Simon Watkins
Internal Examiner
Professor
Department of Physics

Date Defended: 01 May 2015

Abstract

Silicon has been the backbone of the microelectronics industry for decades. As spin-based technologies continue their rapid development, silicon is emerging as a material of primary interest for a number of these applications. There are several techniques that currently exist for polarizing the spin-$\frac{1}{2}$ ^{29}Si nuclei, which account for 4.7% of the isotopic makeup of natural silicon (the other two stable isotopes, ^{28}Si and ^{30}Si, have zero nuclear spin). Polarized ^{29}Si nuclei may find use in quantum computing (QC) implementations and magnetic resonance (MR) imaging. Both of these applications benefit from the extremely long T_1 and T_2 of the ^{29}Si nuclear spins. However, the lack of interactions between the ^{29}Si nuclei and their surroundings that allow for these long relaxation times also means that it is difficult to find a source of spin-polarization that effectively couples to the ^{29}Si spin ensemble. We identify and exploit a field-dependent, frequency-matched resonant transfer process between ^{31}P donor and ^{29}Si nuclear spins in natural silicon to efficiently hyperpolarize the bulk ^{29}Si to over 6%. This all-optical technique requires no microwave irradiation, and the coupling can be switched off to recover the ultra-long nuclear spin relaxation lifetimes of ^{29}Si. This switchable hyperpolarization technique significantly enhances the usefulness of ^{29}Si spins in QC and MR imaging applications.

Keywords: Silicon; silicon-29; phosphorus-31 donors; hyperpolarization; donor bound excitons; magnetic resonance detection

Acknowledgements

I have many, many people to thank for their expertise, advise, friendship, and emotional support throughout this degree. First of all, I must express my deep gratitude to my senior supervisor, Mike Thewalt, for supporting me financially and contributing so much of his knowledge and prowess to this project. His experimental intuition and knowledge of the physical systems under question are extraordinary and give me something to strive towards. It is also my pleasure to acknowledge Stephanie Simmons and to give her credit for the genesis of this idea and the mentorship she has provided me from abroad as we carried out the experiments here at SFU. Her enthusiasm and drive are unmatched, and when she was able to visit, she never failed to inspire me. Thanks to both of you for mentoring me and helping me learn from my (many) mistakes–this has been an invaluable experience.

I was lucky enough to be 'stuck' in the grotto with a fantastic and supportive team of scientists – Jeff, Kevin, Kamyar, and Julian – I have had such a wonderful time working with all of you. A special thank you needs to go out to Jeff for all the emotional support he provided, and the huge amount of physics I was able to understand and more truly appreciate through our numerous exhilarating conversations. That spark of understanding keeps me passionate about physics. Finally, I need to thank my Mom, Dad, and brother for always believing in me and for helping shape who I have become throughout my life. I love you all so much. Thank you for pouring everything you have into me. And to everyone else, from my amazing life-long friends and support system in Chicago to all the magical people I have met in the beautiful city of Vancouver, thank you for everything – you know who you are and everything you have done.

Table of Contents

List of Figures

Chapter 1

Introduction

Due to the incredible success of the microelectronics industry, the silicon manufacturing process has become extraordinarily well developed. Because of this, silicon is a quintessential material when considering any future applications of semiconductors in science and technology. The size of transistors in computer processors has steadily decreased and quantum effects have become more important in these devices [1]. Related to this, scientists have been considering the possibility of using the quantum properties of silicon, as well as the dopant impurities it may contain, as a primary platform for future technologies [1, 2].

This thesis work focuses on the silicon-29 (^{29}Si) isotope, the only stable isotope of Si that possesses a non-zero nuclear spin. In this work we develop a technique to hyperpolarize ^{29}Si nuclear spins, inducing a nuclear polarization far larger than the polarization achievable under easily realized thermal equilibrium conditions. This chapter will give a short background of ^{29}Si hyperpolarization techniques that have already been developed and will discuss the two primary applications this procedure is likely to influence the most.

1.1 ^{29}Si Nuclear Polarization

Scientists first began working on techniques of nuclear hyperpolarization for applications in high energy particle physics and low energy nuclear physics [3]. These methods became known as dynamic nuclear polarization (DNP) experiments. Even though the nuclear polarizations required (>20%) [4] for use as polarized targets in high energy physics experiments were never achievable in silicon [3], these techniques were incorporated into studies of the fundamental dynamics of semiconductors. In silicon, DNP has been used to study the interaction of conduction electrons [5, 6], different species of impurities and lattice defects [7, 8], and static magnetic fields [9] with the host ^{29}Si nuclear spins in the Si lattice. Additionally, by looking at the ^{29}Si polarization and relaxation dynamics scientists have been able to better understand the effects that illumination [10, 11], crystal deformation [12], high dopant concentration [13], isotopic concentration [14, 15], and micro- and nanoparticles [16, 17] have on a variety of properties of silicon. These properties include the nuclear magnetic resonance properties of ^{29}Si and impurity centres, the spin resonance properties of electrons bound to impurities, and the polarization of electrons in the conduction band.

Due to conservation laws, all DNP techniques require a reservoir of polarization to transfer to the target nuclei. A variety of techniques to hyperpolarize ^{29}Si have been developed. The majority of these have used the sizeable thermal polarization of unpaired electron spins at low temperatures and high magnetic fields as the reservoir of polarization. These unpaired electrons can be associated with donors [3, 15, 13], defect states (on the surface or in the crystal bulk) [12, 16, 17], or conduction electrons [10, 18]. Each of these sources requires a direct interaction between the electrons and ^{29}Si nuclei to drive mutual spin flips that will polarize the ^{29}Si. The most successful techniques to date have used oscillating magnetic fields at microwave frequencies [16, 15, 13, 17] to drive the mutual spin flips of the coupled electron-nuclear spin system. This can be done directly, by driving forbidden microwave transitions, a technique called the solid effect [3]. Conversely, by using microwaves to equalize the electron spin up and spin down populations under conditions where there should otherwise be a non-zero equilibrium polarization of the unpaired electronic spin states, one can throw the electron ensemble system out of equilibrium. This leads to the electron relaxing via mutual spin flips with the ^{29}Si, a method of polarizing the ^{29}Si called the Overhauser Effect [3]. Using the Overhauser Effect, Dementyev, *et al.* have been able to generate a ^{29}Si hyperpolarization of $\sim 10\%$ [13]. Scientists have also attempted to use optical pumping [10, 12, 18] to put electrons in a non-thermal state and hyperpolarize the ^{29}Si by relying on relaxation processes that entail mutual spin flips. However, these optical techniques have found less success, generating polarizations of $< 1\%$ [18].

1.2 Applications of ^{29}Si Polarization Methods

There are two primary emergent fields that have been identified as the most likely candidates to benefit from expanding our knowledge of ^{29}Si hyperpolarization techniques. These are the realms of quantum computing (QC) and nanomedicinal applications in magnetic resonance imaging (MRI). For both of these applications, the primary features of hyperpolarized ^{29}Si that make it an attractive medium are its extremely long characteristic spin-lattice relaxation time (T_1), reaching up to 4 hours in bulk Si even at room temperature, and its long characteristic spin-spin dephasing time (T_2). These long relaxation times are due to the lack of other species of spins in Si that can couple to the ^{29}Si and lead to a loss of hyperpolarization.

1.2.1 Quantum Computation

Quantum computation promises dramatic boosts in computing speed by employing quantum algorithms that accomplish crucial tasks, like searching and factoring, much more efficiently than their classical counterparts [19]. In order for a proposed implementation of a quantum processor to be viable, it must satisfy the five Divincenzo criteria [19]:

1. It must be possible to construct a scalable physical system of well-defined qubits;
2. The qubits must be capable of maintaining phase coherence (T_2) for sufficiently long periods of time;
3. There must exist control mechanisms such that one can perform unitary transformations on the qubits that correspond to a universal set of quantum gates;
4. Each qubit state needs to be able to be measured with high fidelity, and
5. The qubits must be able to be initialized into a simple state (e.g. $|000\ldots\rangle$) at the beginning of the calculation.

There have been several QC proposals [20, 21, 22] that use chains of ^{29}Si nuclei embedded in a spin-free host lattice of enriched ^{28}Si as an analogue to the molecules used in liquid state nuclear magnetic resonance (NMR) QC implementations [23, 24]. Itoh [25] provides the details of how linear chains of ^{29}Si in ^{28}Si meet the five criteria listed above that are required for an effective QC implementation. These criteria are summarized below.

To satisfy criterion one, it must be easy to scale the construction of these ^{29}Si chains. Long chains can be fabricated by depositing atoms of ^{29}Si on a ^{28}Si crystal that has been specially designed to have a terrace-like surface. This organizes the deposited atoms into chains along each step [25]. The ability of ^{29}Si nuclear spins to satisfy criterion two is one of the primary reasons they are being considered as a qubit candidate. The T_2 of ^{29}Si has been shown to be very long. When using techniques that effectively decouple nearby ^{29}Si nuclear spins from each other to reduce dephasing, ^{29}Si spins can maintain coherence for up to $\sim$25 seconds [26]. To satisfy criterion three, one can achieve universal control of single ^{29}Si spin qubits in linear chains by applying a strong magnetic field gradient to the atoms in the chain and pulsing radio frequency (RF) oscillating magnetic fields at the specific resonant frequency of the desired qubit in the field gradient. The dipole-dipole interaction between qubits can also be controlled with decoupling pulse sequences to perform multiple qubit quantum operations [25, 27]. To read out the spin state of a ^{29}Si qubit in this QC implementation as required by four, Itoh [25] suggests using electrons bound to ^{31}P donors at the ends of the ^{29}Si chains to probe the spin state of the ^{29}Si qubit [28] using the highly anisotropic hyperfine interaction it exhibits with nearby ^{29}Si nuclear spins [29].

This thesis is concerned with addressing the fifth criterion. The technique we have developed, as well as the DNP techniques discussed above in section 1.1, allow one to initialize a large fraction of the ^{29}Si spin qubits into the same state. The ^{31}P donors needed to read out the ^{29}Si spin states in this sort of implementation can also act as a reservoir of hyperpolarization to initialize the ^{29}Si. The ^{29}Si spins nearest the donors will polarize first, and the induced spin polarization will diffuse along the chains of nuclei [14, 15, 13]. This ability to effectively initialize the qubits is a huge improvement on the very small polarization values and strongly mixed initial states characteristic of liquid state NMR implementations of QC. This inability to effectively initialize the qubits in liquid state NMR QC limits the maximum number of qubits that can be added to the system while maintaining a high signal to noise ratio, making it unscalable.

1.2.2 Direct MRI of Micro- and Nanoparticles

MRI is a medical imaging technique that has become widely used in diagnosing illness. It uses high static magnetic fields and radio-frequency (RF) oscillating magnetic fields to probe nuclei in the body. The signal that is detected in MRI requires the existence of polarized nuclear spins. Because the equilibrium polarization of nuclear spins at room temperature is low and scales with the applied magnetic field strength, high fields are required. However, even at the maximum applied magnetic field commercial MRI machines are typically able to achieve (~ 7 T), these polarization values are still typically only of order 10^{-5}. This high field requirement can be relaxed by injecting imaging agents spin-polarized beyond equilibrium (a technique known as hyperpolarization) into the body and using MRI to image the agents directly. This has been achieved using hyperpolarized noble gases to image the lungs [30, 31], hyperpolarized ^{13}C in metabolites to monitor tumor responses to treatment [32], and hyperpolarized ^{29}Si in silicon microparticles in a variety of *in vivo* environments [17]. To be an effective medical imaging agent, there are three primary requirements. First, the imaging agent must be biocompatible (safe to administer). Second, there must exist a source of spin polarization that can be transferred to the target nuclei. Third, the nuclei being imaged must have long spin-lattice relaxation times (T_1) to maintain hyperpolarization in the tumultuous *in vivo* environment throughout the imaging procedure.

Hyperpolarized ^{29}Si in micro- and nanoparticles made out of silicon possess the required characteristics listed above and, in addition, a number of other advantageous properties. In tests on mice, the Si micro- and nanoparticles appear to be biocompatible [17]. The magnetic moment of ^{29}Si is similar to ^{13}C and ^{15}N, putting its resonance within the tuning range of most commercial multi-nuclear MRI machines [17]. Additionally, there are naturally only trace quantities of silicon in the body, meaning that imaging the silicon particles is essentially background-free. In bulk silicon, ^{29}Si nuclear spins have also been shown to have T_1 relaxation times that exceed four hours at room temperature [33, 34]. ^{29}Si exists in a mostly spin-free lattice with a natural abundance of $\sim 4.7\%$. The nuclei exhibit a weak dipole-dipole interaction with each other and have no electric quadrupole moment, making them insensitive to stray crystalline electric fields. Combined with the isotropic nature of the silicon lattice, these properties make any spin polarization insensitive to lattice orientation [35, 17] and allow these long T_1 relaxation times to persist even when tumbling through space, as in a fluid suspension [35], and in weak magnetic fields [36]. To that effect, *in vivo* relaxation time measurements of ^{29}Si in natural silicon ($^{\mathrm{nat}}$Si) microparticles have shown a ^{29}Si $T_1 \approx 40$ minutes [17]. Using a ^{29}Si hyperpolarization technique developed by Dementyev, *et al.* [16] that uses unpaired electrons bound to defects on the surface of the microparticles, the positive attributes of Si microparticles outlined above have proven to be effective enough to achieve direct MRI of these particles *in vivo* [17].

1.2.3 ^{29}Si Hyperpolarization Via Switchable Dipole-Dipole Coupling

Maintaining long ^{29}Si T_1 and T_2 relaxation times is crucial when initializing ^{29}Si nuclear spins for use in QC, as well as when preparing hyperpolarized silicon micro- or nanoparticles for imaging. However, introducing large numbers of unpaired electrons coupled to the ^{29}Si for hyperpolarization simultaneously acts as a source of relaxation, reducing the T_1 and T_2 times. Hence, it is of interest to identify a source of ^{29}Si hyperpolarization where the coupling used to transfer polarization to the ^{29}Si can be switched off to recover the long relaxation times that give these applications promise.

The idea for this project was developed by Stephanie Simmons with the hope that we could create a switchable technique for ^{29}Si hyperpolarization. At Simon Fraser University, we carried out a series of experiments to bring this idea to fruition. To that effect, we have developed an all-optical method of hyperpolarizing ^{29}Si to over 6% in bulk $^{\mathrm{nat}}$Si. This method uses optically hyperpolarized ^{31}P donor nuclear spins as the reservoir of hyperpolarization. The ^{31}P nuclear hyperpolarization is able to diffuse to nearby ^{29}Si nuclei through a strongly field dependent dipole-dipole coupling mechanism. This field-dependence allows us to switch off the ^{31}P-^{29}Si coupling when the hyperpolarization procedure is complete to recover the long ^{29}Si relaxation times. We believe this is the highest ^{29}Si nuclear polarization achieved by an all-optical technique to date.

Chapter 2

Theoretical Framework

This chapter will first discuss the basic concepts required to understand the silicon crystal and donor impurities. It will then give a general description of nuclear spin hyperpolarization and how this could be implemented in a diamagnetic crystal containing dilute paramagnetic impurity centres, as is the case for a natural silicon ($^{\mathrm{nat}}$Si) crystal dilutely doped with phosphorus-31 (^{31}P) donor impurities.

2.1 The Silicon Crystal

Crystalline silicon forms a diamond lattice structure, where each atom sits at the centre of a tetrahedron constructed from its four nearest neighbours [37]. As seen in Fig. 2.1, the diamond lattice structure can be constructed from a face centred cubic lattice with a two atom basis such that one is located at (0,0,0) and the other is at the position $(\frac{a}{4}, \frac{a}{4}, \frac{a}{4})$, corresponding to one quarter of the diagonal length of the unit cell along the [111] lattice direction. In Si, the lattice constant $a = 5.43$ Å [38], as indicated in Fig. 2.1. Si has 14 protons and is a group-IV element with three stable isotopes. In $^{\mathrm{nat}}$Si, these are: ^{28}Si with a concentration of $\sim 92.2\%$, ^{29}Si with a concentration of $\sim 4.7\%$, and ^{30}Si with a concentration of $\sim 3.1\%$ [39]. ^{28}Si and ^{30}Si both have a nuclear spin of zero, while ^{29}Si has a nuclear spin of $\frac{1}{2}$ and will couple to other spin systems through contact hyperfine and dipole-dipole interactions.

Silicon is an indirect bandgap semiconductor with a energy gap E_g between the maximum of the valence band and the minimum of the conduction band of $E_g = 1.17$ eV at 4.2 K [41]. Since the bandgap is indirect, the maximum energy of the valence band occurs at a different position in $\mathbf{k}$-space than the minimum of the conduction band. Fig. 2.2 shows a diagram of the band structure in silicon along the [001] direction. The energy of the valence band is maximum at the the Brillouin zone centre, where $\mathbf{k} = 0$. The minimum of the conduction band occurs at $\mathbf{k} \approx 0.85\frac{2\pi}{a}$ in the $\langle 100 \rangle$ directions [42]. Hence, Si has six identical conduction band minima [37]. The Si valence band is split, as seen in Fig. 2.2, due

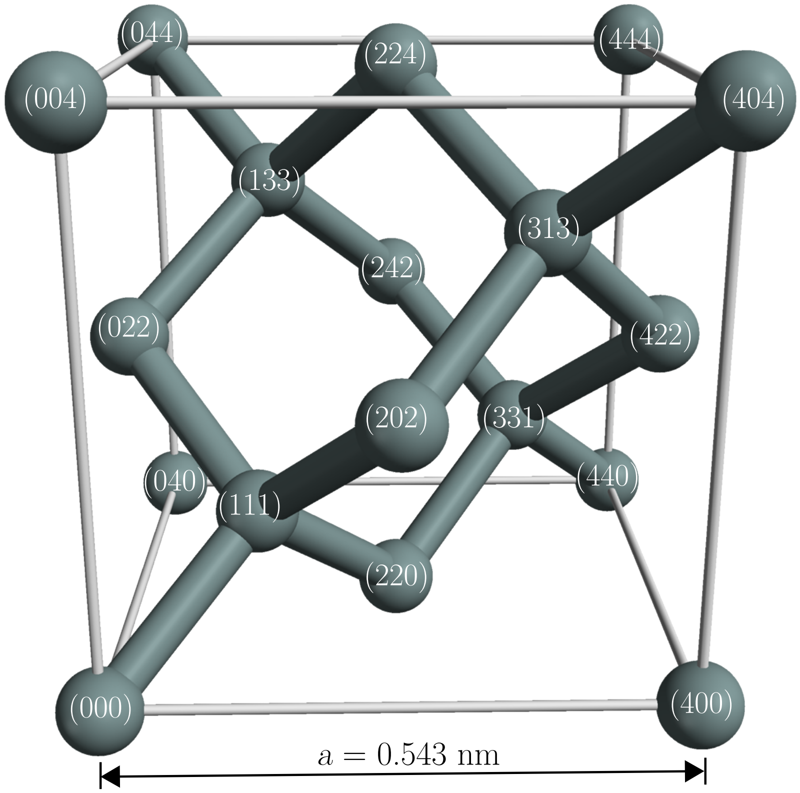

Figure 2.1: The silicon unit cell. Lattice sites are labeled in units of $(\frac{a}{4}\frac{a}{4}\frac{a}{4})$, with $a = 0.543$ nm the size of the silicon unit cell. Figure adapted from [40].

to the interaction of holes with the lattice. Holes have spin angular momentum $J_h = \frac{3}{2}$ and holes with different magnetic quantum numbers ($m_h = \pm\frac{1}{2},\ \pm\frac{3}{2}$) have different effective masses. Holes with $m_h = \pm\frac{1}{2}$ are referred to as light holes, while those with $m_h = \pm\frac{3}{2}$ are referred to as heavy holes. Each type of hole (light or heavy) has a gyromagnetic ratio strongly dependent on the crystal orientation in the applied magnetic field.

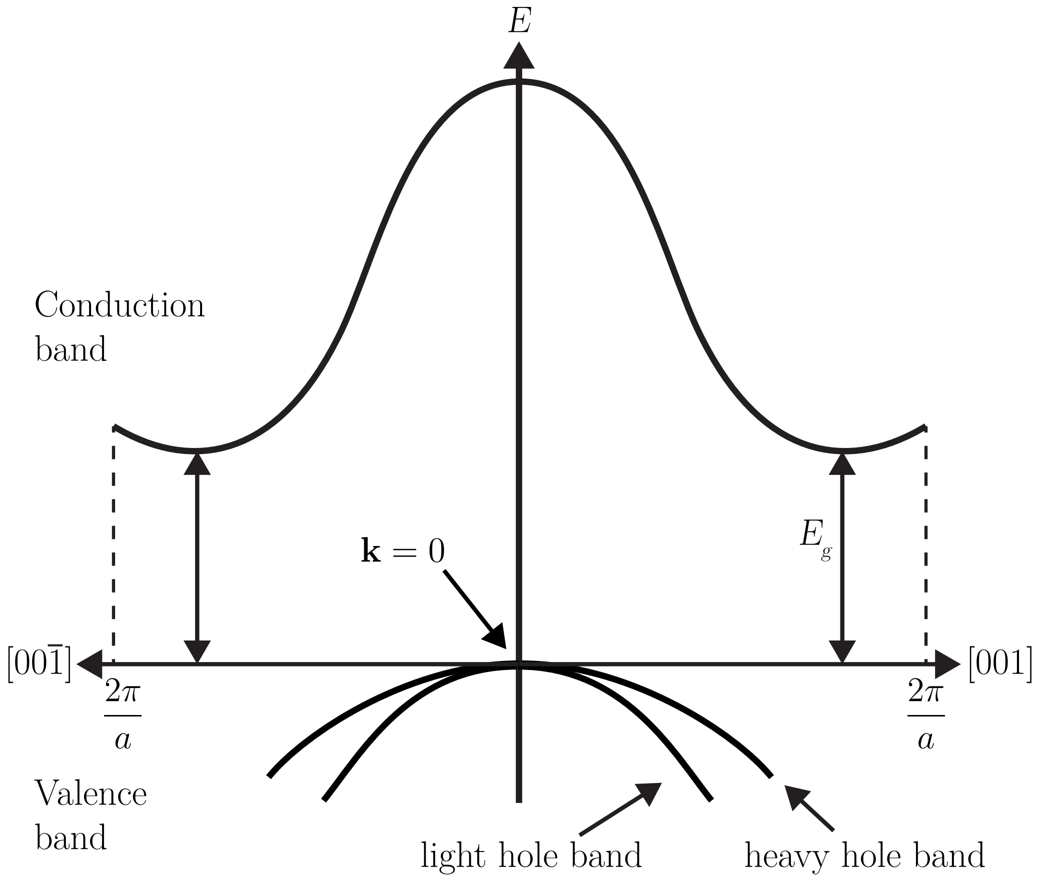

Figure 2.2: A schematic illustration of the silicon band structure along the [001] directions. Because of the symmetry of the lattice, this same conduction band minima exist along all the [100] and [010] directions. Since silicon is an indirect bandgap semiconductor, a wavevector conserving phonon must be created when an electron is excited from the valence band maximum to the conduction band minimum. At 4.2 K $E_g = 1.17$ eV [41]. Figure adapted from [43].

2.2 Phosphorus Donor Impurities

Phosphorus is a common impurity atom found in silicon. It is a substitutional impurity, meaning that it replaces one of the silicon atoms in the lattice while maintaining all the chemical bonds with the surrounding four silicon atoms. Phosphorus possesses only one stable isotope, ^{31}P, and is a group-V element with atomic number 15. Because it has five valence electrons compared to the four of Si, neutral ^{31}P impurities in the silicon lattice will donate an electron (this is the reason ^{31}P is called a 'donor impurity'). As a substitutional donor, 4 of the ^{31}P impurity's valence electrons will be used in covalent bonds with the neighboring Si atoms, leaving the extra 'donated' electron to experience a screened, attractive Coulomb potential due to the nucleus. At low temperatures, this potential loosely binds the donor's electron with an energy of ~ 45.6 meV below the conduction band in hydrogenic orbitals. At temperatures above $\sim$30 K, the ^{31}P donors will begin to ionize and at room temperature they will be completely ionized. This makes ^{31}P neutral donors (D^0) inherently low temperature systems [44, 45].

For a D^0 in its 1s-like ground state, the maximum value of the donor electron wavefunction is at the nucleus of the donor impurity and a Fermi contact hyperfine interaction is present between the two particles. This interaction is governed by the donor electron hyperfine tensor $\mathbf{A}$, which at the donor nucleus is an isotropic scalar with a value of $A = 117.53$ MHz for ^{31}P [42]. At low temperatures and under an applied static magnetic field $\mathbf{B}_0 = B_0\hat{z}$, this coupled system can be described by the ^{31}P donor hyperfine Hamiltonian

$$\begin{aligned}\hat{H} =& \gamma_e\hat{\mathbf{S}}\cdot\mathbf{B}_0 - \gamma_I\hat{\mathbf{I}}\cdot\mathbf{B}_0 + A\hat{\mathbf{I}}\cdot\hat{\mathbf{S}}\\ =& \gamma_e\hat{S}_zB_0 - \gamma_I\hat{I}_zB_0 + A\hat{\mathbf{I}}\cdot\hat{\mathbf{S}}\ ,\end{aligned} \tag{2.1}$$

where $\hat{\mathbf{S}} = \begin{pmatrix}\hat{S}_x & \hat{S}_y & \hat{S}_z\end{pmatrix}^{\mathrm{T}}$ and $\hat{\mathbf{I}} = \begin{pmatrix}\hat{I}_x & \hat{I}_y & \hat{I}_z\end{pmatrix}^{\mathrm{T}}$ with the T superscript signifying the transpose of these row vectors. The donor electron and nuclear gyromagnetic ratios are $\gamma_e = g_e\mu_B = 28.020\ \mathrm{MHz}\cdot\mathrm{mT}^{-1}$ and $\gamma_I = g_I\mu_I = 17.247\times10^{-3}\ \mathrm{MHz}\cdot\mathrm{mT}^{-1}$, where g_e and g_I are the phosphorus donor electron and nuclear g-factors and μ_B and μ_I the Bohr and nuclear magnetons, respectively [46, 47].

At $B_0 = 0$, the hyperfine interaction term $A\hat{\mathbf{I}}\cdot\hat{\mathbf{S}}$ splits the energies of the $\hat{\mathbf{F}} = \hat{\mathbf{I}}+\hat{\mathbf{S}} = 1$ triplet and $\hat{\mathbf{F}} = \hat{\mathbf{I}} - \hat{\mathbf{S}} = 0$ singlet two particle spin states by the energy of the hyperfine interaction constant A. Under an applied magnetic field, the donor electron spins states are split according to the Zeeman interaction $\gamma_e\hat{S}_zB_0$. Similarly, in the presence of a magnetic field, the donor nuclear spin splits the electron spin states into hyperfine states with the $-\gamma_I\hat{I}_zB_0$ term. In addition to splitting the energies of the zero field spin states, $A\hat{\mathbf{I}}\cdot\hat{\mathbf{S}}$ importantly causes the energy difference (also called the Larmor frequency) between the ^{31}P nuclear spin states to be dependent on the state of the donor electron spin. Hence, the ^{31}P nuclei will possess distinct nuclear magnetic resonance (NMR) frequencies depending on the state of the donor electron. Because of this, throughout this thesis we will distinguish the two different Larmor frequencies of the ^{31}P nuclei by referring to whether the coupled electron spin is in the $|\uparrow\rangle$ or $|\downarrow\rangle$ state (see Fig. 2.3 for an illustration of this).

We can determine the energy levels of this coupled spin-$\frac{1}{2}$ system from the Hamiltonian using the Breit-Rabi formula [48]. At high field, the eigenstates can be accurately approximated by $|\uparrow\Uparrow\rangle$, $|\uparrow\Downarrow\rangle$, $|\downarrow\Downarrow\rangle$, $|\downarrow\Uparrow\rangle$, where the first arrow ($\updownarrow$) corresponds to the electron spin state and the second arrow ($\Updownarrow$) to the nuclear spin state. We will label these states $|1\rangle$, $|2\rangle$, $|3\rangle$, $|4\rangle$ in order of decreasing energy when $B_0 < 3.4$ T (the field region we will be operating at in this study), as shown in Fig. 2.3. These energies are given by [48, 49]

$$\begin{aligned}
E_{|\uparrow\Uparrow\rangle} = & E_1 = \frac{A}{2}\left\{\frac{1}{2} + \frac{B_0(\gamma_e - \gamma_I)}{A}\right\} \\
E_{|\uparrow\Downarrow\rangle} = & E_2 = \frac{A}{2}\left\{-\frac{1}{2} + \sqrt{\left[\frac{B_0(\gamma_e + \gamma_I)}{A}\right]^2 + 1}\right\} \\
E_{|\downarrow\Downarrow\rangle} = & E_3 = \frac{A}{2}\left\{\frac{1}{2} - \frac{B_0(\gamma_e - \gamma_I)}{A}\right\} \\
E_{|\downarrow\Uparrow\rangle} = & E_4 = \frac{A}{2}\left\{-\frac{1}{2} - \sqrt{\left[\frac{B_0(\gamma_e + \gamma_I)}{A}\right]^2 + 1}\right\} \ .
\end{aligned} \tag{2.2}$$

Since A defines the donor electron-nuclear interaction energy, the relation $(E_1 - E_4) - (E_2 - E_3) = A$ holds for all B_0.

In low magnetic fields, $|\uparrow\Downarrow\rangle$ and $|\downarrow\Uparrow\rangle$ are only approximate eigenstates of the Hamiltonian and hyperfine mixing occurs between them, whereas $|\uparrow\Uparrow\rangle$ and $|\downarrow\Downarrow\rangle$ are pure eigenstates. When $\gamma_e B_0 \gg A$, $|\uparrow\Downarrow\rangle$ and $|\downarrow\Uparrow\rangle$ will be sufficiently pure to be considered eigenstates of the Hamiltonian. Since $\gamma_e = 28.020\ \mathrm{MHz}\cdot\mathrm{mT}^{-1}$, in a field of just 50 mT, $\gamma_e B_0 = 1397.85$ MHz is over two orders of magnitude larger than A. Under a projective measurement of the electron or nuclear spin in the $|\uparrow\Downarrow\rangle$ or $|\downarrow\Uparrow\rangle$ states at 50 mT, the probability of returning the opposite admixed state is negligibly small: $|\pm 0.042|^2 = 0.0018$ [49]. In this work, we will be operating at fields above 2 T where $|\uparrow\Downarrow\rangle$ and $|\downarrow\Uparrow\rangle$ are pure enough to be considered eigenstates of the Hamiltonian given in Eq. 2.1.

2.2.1 Donor Bound Excitons

Illumination from sub-bandgap light ($\hbar\omega < E_g$) at specific energies corresponding to an approximate wavelength of 1078 nm will create electron-hole pairs localized around the donor impurities called donor bound excitons ($\mathrm{D}^0\mathrm{X}$, in contrast to D^0). $\mathrm{D}^0\mathrm{X}$ states can also be formed by capturing free excitons (FE) onto D^0. FE are bound electron-hole pairs that are created when when the sample is illuminated with above-bandgap light. An illustration of the initial (D^0) and final ($\mathrm{D}^0\mathrm{X}$) states of these near infrared optical absorption transitions is shown in Fig. 2.4B.

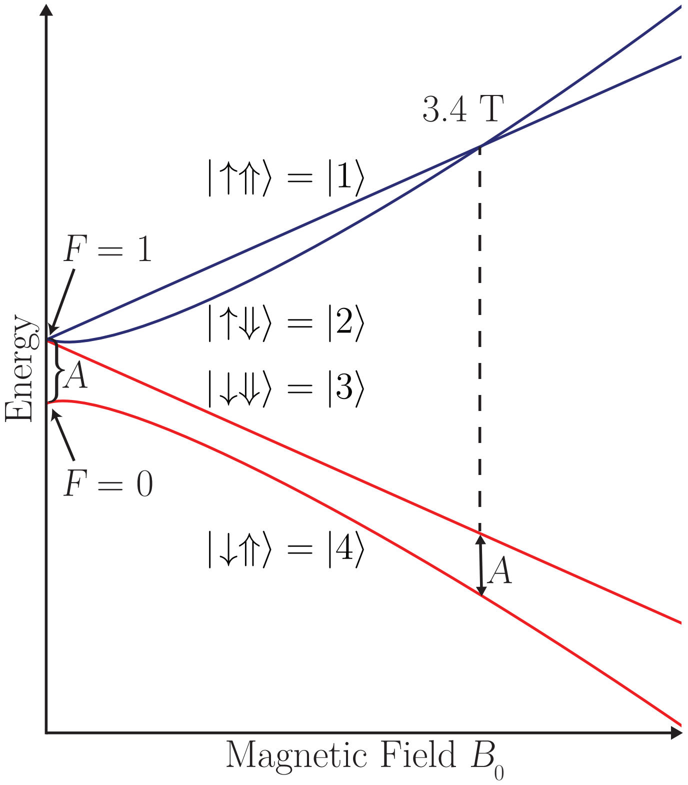

Figure 2.3: This schematic diagram depicts the important features of the coupled donor electron and nuclear spin energy levels as a function of static magnetic field strength B_0. Note that at $B_0 = 0$, the splitting between the $F = 1$ and $F = 0$ states is equal to the donor electron contact hyperfine interaction energy at the nucleus, $A = 117.53$ MHz. Additionally, at $\sim$3.4 T the energies of $|\uparrow\Uparrow\rangle$ and $|\uparrow\Downarrow\rangle$ cross and the Larmor frequency of ^{31}P nuclei with electron spin $|\downarrow\rangle$ is equal to A.

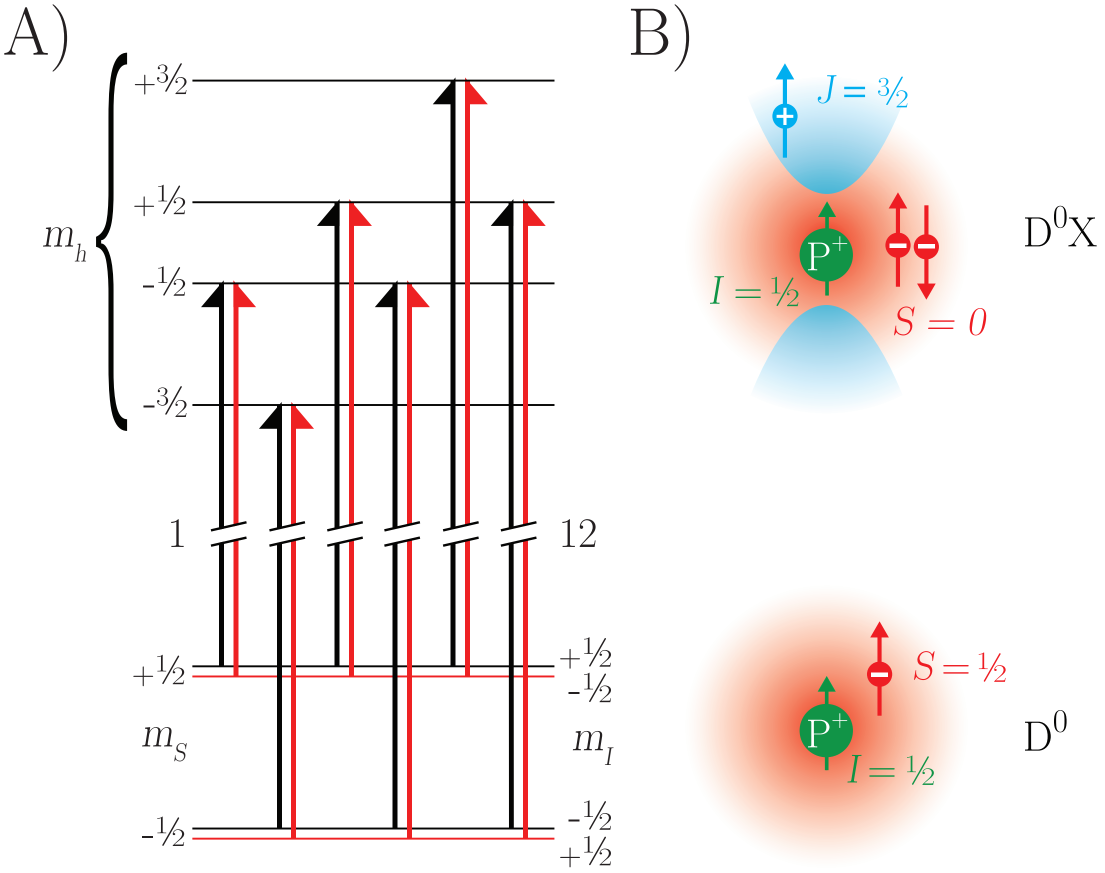

Figure 2.4: A diagram of the 12 allowed ^{31}P D^{0}X absorption transitions. A) shows the initial and final states of the 12 allowed D^{0}X transitions in ^{31}P. Because the g-factor of the hole states is highly dependent on the orientation of the crystal relative to $\mathbf{B}_0$, the energies of these transitions depend not only on the magnitude of B_0, but also on the sample orientation. B) shows an illustration of the initial and final states when creating bound excitons in ^{31}P. The electrons, both in D^0 and D^{0}X (where they form a singlet state), have an s-like wavefunction (depicted in pink), while the hole possesses a probability amplitude characteristic of a p-like wavefunction (depicted in blue). Figure adapted from [50].

Since the two electrons are in a singlet state ($S = M_S = 0$), there is no hyperfine interaction present between them and the hole, or donor nucleus. Additionally, this hole possesses a *p*-like wave function, with zero probability amplitude at the site of the donor nucleus. Therefore, there is no spin interaction between the hole and the nucleus (see Fig. 2.4B). Holes have spin $J = \frac{3}{2}$, and under the applied magnetic field the four-fold m_h degeneracy will be lifted as the states split according to the Zeeman interaction. Ignoring the negligible bare nuclear Zeeman energy, the energy levels of the $\mathrm{D^0X}$ states in an applied magnetic field are given solely by the four hole spin states described by the Hamiltonian

$$\hat{H} = g_h \mu_B \hat{J}_z B_0 \ , \tag{2.3}$$

where the g_h is the hole *g*-factor, which is different for the light ($m_h = \pm\frac{1}{2}$) and heavy ($m_h = \pm\frac{3}{2}$) holes and is strongly dependant on the crystal orientation relative to $\mathbf{B}_0$.

The lifetime of a phosphorus $\mathrm{D^0X}$ is ~ 280 ns [51]. When the bound exciton decays, one of the two electrons in the spin-singlet will recombine with the hole, releasing energy triggering one of two possible outcomes. The most likely outcome is that the energy released will ionize the electron that made up the other half of the singlet (a process called Auger recombination). However, with an efficiency of $\sim 10^{-4}$, this recombination event will release a photon through either a phonon-assisted or no-phonon process [51]. The existence of this small amount of luminescence allows the impurity content of the silicon sample to be characterized by examining the energies of the sharp bound exciton lines that exist at sub-bandgap energies in photoluminescence (PL) spectra [52].

Under an applied magnetic field, there are 12 allowed $\mathrm{D^0X}$ transitions for phosphorus such that the total change in the angular momentum $\Delta M = \Delta m_S + \Delta m_h = \pm 1$ or 0 (the possible quanta of spin angular momentum a photon can have, in units of $\hbar$), as seen in Fig. 2.4A. Using photoluminescence excitation spectroscopy, a tunable laser can be scanned across the energies of the transitions from the $\mathrm{D^0}$ states to the $\mathrm{D^0X}$ states while a detector monitors either the luminescence photons or the change in impedance of the sample as the Auger recombination process ionizes electrons into the conduction band. In isotopically enriched ^{28}Si, all 12 of these $\mathrm{D^0X}$ transitions can be resolved with a linewidth of approximately 37 MHz. This makes it possible to achieve selective excitation of the electron and nuclear spin states of the ^{31}P donors [53, 54]. However, in a $^{\mathrm{nat}}$Si sample, the $\sim 4.7\%$ isotopic concentration of ^{29}Si and 3.1% concentration of ^{30}Si isotopes significantly broaden these optical transitions to the point where all resolution of the nuclear hyperfine components is lost. Only at high magnetic fields (~ 1 T) is electron spin state dependent excitation of $\mathrm{D^0}$ to $\mathrm{D^0X}$ in phosphorus-doped natural silicon (^{31}P:Si) possible [39].

2.2.2 Relaxation Processes in ^{31}P

When a spin ensemble is polarized out of its equilibrium population distribution, the system tends toward thermal equilibrium. The channels that allow for these systems to settle into their equilibrium states are called relaxation processes. In the spin system described in this thesis, these relaxation processes are associated with energy exchange with the Si crystal lattice, free carriers, and other spins and impurities. As illustrated in Fig. 2.5 below, there are three important relaxation mechanisms to consider when working with neutral ^{31}P donors in Si: the electron, cross, and nuclear spin-lattice relaxation processes with characteristic time scales T_{1e}, T_{1x}, and T_{1n}, respectively [55]. Since these relaxation processes all occur in spin systems, they must conserve spin angular momentum in addition to energy. Because of this, relaxation between $|\uparrow\Uparrow\rangle$ and $|\downarrow\Downarrow\rangle$ is extremely improbable, as $\Delta M = \pm 2$, and will not be considered [55].

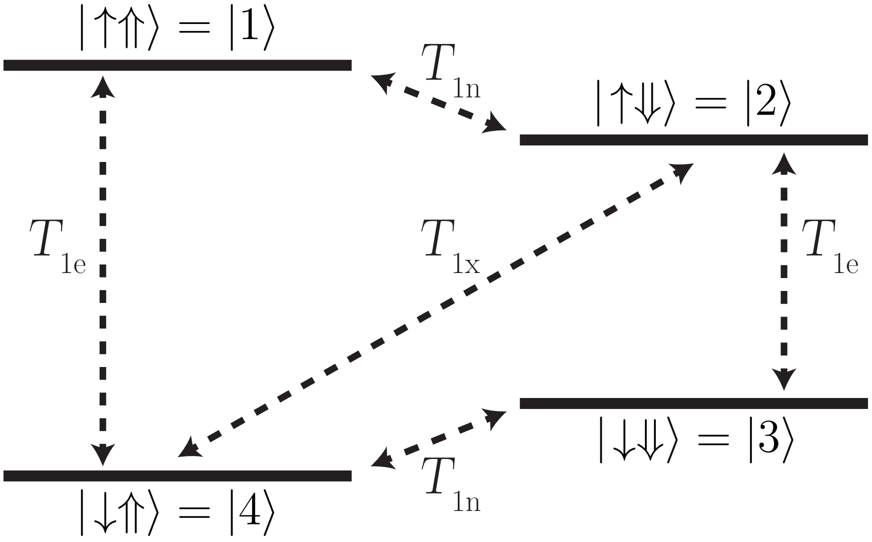

Figure 2.5: This diagram illustrates the possible D^0 spin-lattice relaxation channels in ^{31}P.

There are a number of parameters that determine how energy exchange with the lattice occurs [55, 56] so pinning down the actual mechanisms behind the neutral ^{31}P relaxation processes is difficult. However, it has been found that these T_1 times and the mechanisms behind them depend on many parameters, including the temperature, applied magnetic field, and impurity concentration [55, 57, 58, 59, 60].

When a hyperpolarized spin ensemble relaxes via energy exchange with the lattice, the target state's surplus population is reduced. Any hyperpolarization technique must fight against spin lattice relaxation to maintain the desired non-equilibrium population distribution. However, in a coupled two-particle spin system, T_1 relaxation processes that involve a spin flip of each element (like T_{1x}) can be exploited to effectively drive the population for one of the coupled particles into a desired spin state. This phenomenon is called the Overhauser Effect and will be introduced more completely in section 2.3.2.

2.3 Spin Polarization

One of the parameters that can be examined and manipulated when working with a system made up of an ensemble of spins is the polarization of that spin system. The polarization of an ensemble of two-level systems is the population difference $N_b - N_a$ as a fraction of the total population of the ensemble $N_b + N_a$. When a system is in thermal equilibrium at a finite temperature, any time there is an energy splitting between quantum states there will be some degree of excess population in the lower energy state of the quantum system. To determine the equilibrium polarization P_0 of a two level system made up of states $|a\rangle$ and $|b\rangle$, with an energy difference $\Delta E_{ba} = E_b - E_a < 0$, at an absolute temperature T, we can use [61]

$$P_0 = \frac{1 - e^{\frac{\Delta E_{ba}}{k_B T}}}{1 + e^{\frac{\Delta E_{ba}}{k_B T}}} \ . \tag{2.4}$$

In general, a higher ΔE_{ba} and/or lower absolute temperature leads to a higher P_0 [61].

In this thesis, all discussion of polarization will refer to the polarization of a spin ensemble. The polarization of a spin ensemble can be manipulated from the equilibrium polarization by supplying additional energy to the system. The energy required to manipulate state populations or generate hyperpolarized states often takes the form of electromagnetic radiation. The forms of polarization manipulation discussed in this thesis are near-infrared optical excitation to create hyperpolarized donor electron spin states and radio frequency (RF) oscillating magnetic fields to coherently manipulate the populations of the nuclear spin states.

2.3.1 Spin Temperature

For any given two level energy splitting ΔE_{ba} and polarization P (not necessarily in equilibrium), we can determine the absolute temperature that would be required to generate this population configuration by solving Eq. 2.4 for T. Hence, we can describe the polarization of a non-equilibrium state relative to thermal equilibrium in terms of temperature.

For example, given the two level system made up of states $|a\rangle$ and $|b\rangle$ with $\Delta E_{ba} = E_b - E_a < 0$ in equilibrium at a temperature T, there will exist a population excess in the lower energy level $|b\rangle$ and a steady state polarization $0 < P_0$. Now, one can apply energy to the system such that the new degree of polarization is P with $P_0 < P$. Since this new situation is equivalent to one where the system is in thermal equilibrium at a lower temperature, this is referred to as a cold spin temperature relative to the equilibrium polarization (a polarization of +1 would correspond to a spin temperature of absolute zero).

On the other hand, one can also apply energy to the system such that $0 < P < P_0$. Since this would be equivalent to the system being at a higher temperature, this is referred to as a hot spin temperature. Lastly, the system can be held out of equilibrium so there is a population excess in the higher energy state ($|a\rangle$, in this case) implying $P < 0$. This population distribution is considered to have a negative spin temperature because a negative temperature would be required for Eq. 2.4 to return $P_0 < 0$ [61].

After determining the equilibrium polarization, we can discuss the effectiveness of any polarization technique not only in terms of the difference in population between the states, but also in terms of the enhancement factor the polarization scheme allows us to achieve over the equilibrium polarization. The polarization enhancement ϵ is given by:

$$\epsilon = \frac{P}{P_0} \ . \tag{2.5}$$

2.3.2 Nuclear Hyperpolarization Via the Overhauser Effect

In a coupled, two particle spin system in thermal equilibrium with each particle possessing different Zeeman splittings, Eq. 2.4 dictates that the component of the system that has a larger energy splitting will have a higher equilibrium polarization. An example of this situation is the coupled nuclear and electron hyperfine system present in the neutral phosphorus donor under an applied magnetic field. The electron gyromagnetic ratio γ_e is orders of magnitude greater than the nuclear gyromagnetic ratio γ_I and therefore interacts much more strongly with the field. As a result, the donor electron Zeeman splitting is several orders of magnitude larger than the nuclear hyperfine splitting at the fields used in this study. This leads to an extremely large difference between the equilibrium polarization of the two spin species. Using a technique developed by Albert Overhauser called the Nuclear Overhauser effect (NOE) [62] this polarization can be transferred from the electron spins to the nuclear spins by exploiting the coupling between them.

In practice, spin polarization transfer via the NOE is accomplished by holding the polarization of the electron spin system P_e out of equilibrium, usually by driving the $\Delta m_S = \pm 1$, $\Delta m_I = 0$ transitions with some sort of electromagnetic radiation (traditionally with microwave frequency oscillating magnetic fields or, in the case of this study, laser excitation) [63, 64]. T_{1n} is typically orders of magnitude larger than T_{1e} or T_{1x} and is generally neglected when considering the Overhauser hyperpolarization dynamics [65]. T_{1e} acts to bring the system into thermal equilibrium, whereas an AC magnetic field driving electron spin flips acts to saturate the electron spin populations (make the populations of the electron spin $|\uparrow\rangle$ and $|\downarrow\rangle$ states equal). This interplay is characterized by the saturation factor

$$s = 1 - \frac{P_e}{P_0} \ , \tag{2.6}$$

which influences the effectiveness of any nuclear hyperpolarization scheme using the NOE. This parameter acts as a multiplicative factor to the time dependent Overhauser equation

$$\epsilon(t) = 1 + s\frac{|\gamma_S|}{\gamma_I}\left(1 - e^{-t/T_\mathrm{b}}\right) \ . \tag{2.7}$$

Here, T_b is the characteristic time of the Overhauser polarization buildup. Looking at Eq. 2.6, one can see that when driving the NOE with continuous wave (CW) oscillating magnetic fields at microwave frequencies to saturate the electron spin states, s will take on values $0 \leq s \leq 1$. In the limit of infinite microwave power and complete saturation of the electron spin states $P_e = 0 \implies s = 1$. Alternatively, if the electron spins are in thermal equilibrium $P_e = P_0 \implies s = 0$ and Overhauser hyperpolarization becomes impossible. Finally, by creating a negative electron spin temperature, $P_e < 0 \implies 1 < s$ and by examining Eq. 2.7 we can see that this will correspond to an 'enhanced' NOE.

T_1e only influences the Overhauser polarization dynamics by affecting the ratio $\frac{P}{P_0}$ in the definition of s, while relaxation due to T_1x will drive $\Delta m_S = \pm 1$ and $\Delta m_I = \mp 1 \implies \Delta M = \Delta(m_S + m_I) = 0$. Because the T_1x relaxation process involves both an electron and nuclear spin flip, this drives the nuclear polarization into the spin state the electron was in prior to relaxing and vice versa [62, 3].

For example, in the ^{31}P D^0 system, when in equilibrium under a high magnetic field at low temperature, the donor phosphorus electron polarization approaches unity, while the nuclear polarization is still orders of magnitude smaller. If the electron spin population is saturated (hot spin temperature) or inverted (negative spin temperature), T_1x will flip electron spins from $|\uparrow\rangle$ to $|\downarrow\rangle$ [55]. Due to the fact T_1x is a zero quantum transition ($\Delta M = 0$), T_1x will also flip the nuclear spins from $|\Downarrow\rangle$ to $|\Uparrow\rangle$. Over time, this drives the nuclear hyperpolarization of the ^{31}P donors into $|\Uparrow\rangle$. Unfortunately, there is a limit to the maximum nuclear hyperpolarization enhancement ϵ_max possible when saturating the electron transitions. Taking $t \to \infty$ and assuming $s = 1$ in Eq. 2.7 implies

$$\epsilon_\mathrm{max} = 1 + s\frac{|\gamma_e|}{\gamma_I} = 1622 \ , \tag{2.8}$$

for ^{31}P donors in Si. However, one can see that by creating a negative electron spin temperature ($1 < s$), this limit can be surpassed [65].

There are many parameters that affect the efficiency of the nuclear Overhauser effect. One of the most important parameters in the systems this work will be exploring is the thermal population difference between states, something that is greatly influenced by temperature (see Eq. 2.4). The thermodynamic principle of detailed balance tells us that the ratio of populations in two states connected by some rate that moves a fraction of the population from one to the other and vice versa (like spin-lattice relaxation) is equal to the ratio of the two rates that connect the states. Namely, for states $|a\rangle$ and $|b\rangle$ with populations and energies N_a and E_a and N_b and E_b, respectively, connected by rates R_{ab} and R_{ba} that move population from state $|a\rangle$ to $|b\rangle$ and $|b\rangle$ to $|a\rangle$, respectively, the following is true

$$\frac{N_a}{N_b} = \frac{R_{ba}}{R_{ab}} = e^{(E_b - E_a)/k_B T} \ . \tag{2.9}$$

Hence, one can see that by moving to a lower temperature $T_L < T_H$, we can potentially improve the magnitude of the NOE by increasing the relaxation rate ratio. For a constant energy difference $0 < \Delta E_{ab}$ between states $|a\rangle$ and $|b\rangle$ in a coupled electron-nuclear spin system connected by cross relaxation rates R_{ab} and R_{ba}, the ratio of rates that drive the Overhauser hyperpolarization is improved by a factor of

$$\frac{\exp\left(\frac{\Delta E_{ab}}{k_B T_L}\right)}{\exp\left(\frac{\Delta E_{ab}}{k_B T_H}\right)} = \exp\left[\frac{\Delta E_{ab}}{k_B}\left(\frac{1}{T_L} - \frac{1}{T_H}\right)\right] \ . \tag{2.10}$$

2.4 The ^{29}Si Isotope

Out of the three isotopes present in $^{\text{nat}}$Si , the only one that possesses a non-zero nuclear spin is ^{29}Si with a spin of $\frac{1}{2}$. Because the isotope has non-zero nuclear spin, at zero field the energies of the ^{29}Si centres will be degenerate, but under an applied static magnetic field, this degeneracy breaks and the Zeeman energies of the $\pm\frac{1}{2}$ spin states split. This interaction is described by the Hamiltonian

$$\hat{H} = -\gamma_{29}\hat{\mathbf{I}}^{(29)} \cdot \mathbf{B} = -\gamma_{29}\hat{I}_z^{(29)} B_0 \ , \tag{2.11}$$

where $\gamma_{29} = -8.458 \times 10^{-3}$ MHz $\cdot$ mT^{-1} [66]. This creates energy levels (and, therefore, energy level differences) that vary linearly with magnetic field strength.

As previously mentioned, ^{29}Si has an extremely long T_1 and can maintain an S_z eigenstate for up to 3-4 hours at room temperature and for a nearly unmeasurable length of time at liquid helium temperature. There are two principal interaction mechanisms that lead to ^{29}Si spin-lattice relaxation. These are interactions between ^{29}Si nuclear spins and conduction electrons [67, 6] and with donor electrons localized around impurity centres [29]. The latter of the two has been shown to be the most efficient [5, 65, 6].

At room temperature, the Si band gap ($\sim$1.11 eV at room temperature [38]) is several orders of magnitude larger than the thermal energy $k_B T = 25.9$ meV. Therefore, when in the dark at room temperature, there will be few conduction electrons besides those due to ionized D^0. Because there are few conduction electrons even at room temperature and the interaction between them and the ^{29}Si is weak, they contribute only a small portion to the ^{29}Si relaxation rate [6].

At liquid helium temperatures (≤ 4.2 K) in the dark, there are essentially no conduction electrons and the donors will be neutral (D^0). In this situation nearly all of the relaxation is due to interactions with the electrons bound to nearby D^0.

Because the Coulomb interaction between donor nuclei and electrons is screened by the intervening core electrons of the ^{31}P impurity, the donor electron has a wavefunction that is not spatially well-confined. It has an effective Bohr radius of $\sim 20-25$ Å [47, 68]. Hence, the donor electron exhibits an anisotropic hyperfine interaction described by the Hamiltonian

$$\hat{H} = \gamma_e S_z B_0 + \sum_k \left(\hat{\mathbf{I}}_k^{(29)} \cdot \mathbf{A}(\mathbf{r}_k) \cdot \hat{\mathbf{S}} - \gamma_{29} I_{z,k}^{(29)} B_0 \right) \tag{2.12}$$

with the ~ 80 surrounding ^{29}Si nuclei that fall within one Bohr radius. The tensor $\mathbf{A}(\mathbf{r}_k)$ describes the anisotropic hyperfine interaction of a donor electron spin with a ^{29}Si nuclear spin situated at lattice site k a distance $\mathbf{r}_k$ as measured from the donor nucleus. In the frame of reference of the electron, these interactions shift its energy levels and manifest themselves as inhomogeneously broadened electron spin resonance (ESR) lines [29]. The donor electron spins have a T_1 that is much shorter than that of the ^{29}Si nuclear spins. Hence, the electrons are seen by the ^{29}Si as a noise bath as they flip up and down randomly on a time scale corresponding to their relaxation rate $1/T_1$ that increases dramatically with temperature. The transition probability of a ^{29}Si nuclear spin flip depends on on the overlap between the wave functions of the donor electron and the ^{29}Si nuclear spin as well as the noise spectrum of the donor electron. The Larmor frequency of the donor electron ω_e is over three orders of magnitude larger than the ^{29}Si Larmor frequency ω_{29}. Therefore, for a donor electron-^{29}Si flip-flop to occur, a large amount of energy must be exchanged with the lattice making the probability of this relaxation transition occurring small. The transition probability per unit time given is by

$$W_{if} = \frac{1}{t}\frac{1}{\hbar^2} \left| \int_0^t \langle m_f | \hat{\mathbf{I}} \cdot \mathbf{A} \cdot \hat{\mathbf{S}} | m_i \rangle \exp\left[\frac{-i(E_f - E_i)t'}{\hbar} \right] \mathrm{d}t' \right|^2 , \tag{2.13}$$

where the hyperfine interaction $\hat{\mathbf{I}} \cdot \mathbf{A} \cdot \hat{\mathbf{S}}$ is treated as a perturbation to the Zeeman components of the donor electron and ^{29}Si two-particle Hamiltonian in Eq. 2.12. $|m_i\rangle$ and $|m_f\rangle$ are the initial and final states of the unperturbed Hamiltonian with corresponding energies E_i and E_f [69].

2.4.1 Spin Diffusion in ^{29}Si

As discussed before, to generate hyperpolarization in an ensemble of nuclear spins, there must be some source of magnetization that generates a non-equilibrium nuclear spin temperature in the surrounding nuclei. This creates a nuclear magnetization (or spin temperature) gradient in the system of coupled nuclear spins. Since each nuclear spin in the ensemble generates a dipole field, nearby nuclear spins interact with each other. When the energy splitting of two nearby nuclei with anti-parallel spins is the same, the exponential term in W_{if} is unity and the transition probability is maximum for a given coupling strength. In this situation, the dipole-dipole coupling between the two spins allow the magnetization to diffuse through the crystal via spin angular momentum and Zeeman energy conserving spin flip-flops ($\Delta m_1 + \Delta m_2 = 0$ and $\Delta E = 0$). Since ^{31}P donor nuclei are easy to hyperpolarize, the spins present in these impurities can be used as the reservoir to generate the hyperpolarization that diffuses through the ^{29}Si via the dipole-dipole interaction they have with each other. The Hamiltonian that describes spin diffusion due to the dipole-dipole interaction [70, 71]

$$\hat{H}_{dd} = d_{ij}\left[4\hat{I}_{iz}\hat{I}_{jz} - (\hat{I}_{i+}\hat{I}_{j-} + \hat{I}_{i-}\hat{I}_{j+})\right] \tag{2.14}$$

with

$$d_{ij} = \frac{\gamma_i \gamma_j \hbar^2}{4|\mathbf{r}_{ij}|^3}(1 - 3\cos^3\theta_{ij}) \ , \tag{2.15}$$

where $\hat{I}_+$ and $\hat{I}_-$ are the nuclear spin raising and lowering operators, respectively, $\gamma_{i,j}$ are the respective gyromagnetic ratios of the two nuclear spins, and θ_{ij} is the angle between $\mathbf{r}_{ij}$ (the vector that separates the two spins) and the applied magnetic field. By examining this Hamiltonian, one can see that the $\hat{I}_{i\mp}\hat{I}_{j\pm}$ terms give rise to the Zeeman energy conserving spin flip-flops between anti-parallel spins that allow for the diffusion of magnetization throughout the lattice. These terms also give rise to the dipole-dipole contribution of the observed ^{29}Si NMR linewidth ν_{dd} [70, 71]. One can determine ν_{dd} experimentally and relate it to the spin-spin relaxation time T_2, which is the characteristic time scale of the interaction that mediates relaxation via dipole-dipole coupling [70, 71]. One can then use T_2 to experimentally estimate this coupling strength. Since, dipole-dipole coupling mediates spin diffusion throughout the crystal, by being able to estimate the strength of this interaction, one can estimate the coefficient that characterizes spin diffusion throughout the crystal bulk [70, 71].

Chapter 3

Experimental Method for ^{29}Si Hyperpolarization

As mentioned in the previous chapter, by using ^{31}P donor impurities in $^{\mathrm{nat}}$Si as easily hyperpolarized sources of magnetization, one can exploit spin diffusion to polarize the ^{29}Si in the bulk of the crystal. This chapter will describe some important characteristics of ^{31}P:Si, and how these properties can be exploited to create a new technique to efficiently hyperpolarize ^{29}Si nuclei. Unlike many ^{29}Si polarization techniques, this method of hyperpolarization does not require strong coupling between unpaired electrons and the ^{29}Si nuclei. Relaxing the requirement that large numbers of coupled, unpaired electrons be added to the material is beneficial to maintaining the long ^{29}Si T_1 times, even at elevated temperatures.

3.1 ^{31}P and ^{29}Si Nuclear Larmor Frequencies

As mentioned in section 2.2, the energy levels in ^{31}P are described via the hyperfine Hamiltonian (Eq. 2.1) and the energies are shown in Eq. 2.2. The contact hyperfine interaction term $A\hat{\mathbf{I}} \cdot \hat{\mathbf{S}}$ in the Hamiltonian makes the energies of the $|\uparrow\Downarrow\rangle$ and $|\downarrow\Uparrow\rangle$ states nonlinear as a function of applied magnetic field. This causes the strong nonlinearity in the ^{31}P nuclear Larmor frequencies seen in both ^{31}P donors with electron spin $|\uparrow\rangle$ and $|\downarrow\rangle$ at low fields (< 60 mT), seen in Fig. 3.1.

^{29}Si nuclei exhibit only a simple nuclear Zeeman interaction under an external magnetic field. This causes both the $|\Uparrow\rangle$ and $|\Downarrow\rangle$ states to be linear in B_0 and gives rise to a Larmor frequency that is linear in B_0, as seen in Fig. 3.1. Because of the nonlinearity in the neutral ^{31}P nuclear Larmor frequency, the Larmor frequency of donors with electron spin $|\uparrow\rangle$ is equal to the Larmor frequency of the ^{29}Si at two fields, as seen in Fig. 3.1. This happens at an applied magnetic field of 2.2835 T with a Larmor frequency of 19.314 MHz when $E_{|\uparrow\Downarrow\rangle} < E_{|\uparrow\Uparrow\rangle}$, and at 6.6800 T with a Larmor frequency of 56.500 MHz, when $E_{|\uparrow\Uparrow\rangle} < E_{|\uparrow\Downarrow\rangle}$. By operating at 2.2835 T, we create a frequency-matched resonance condition between the

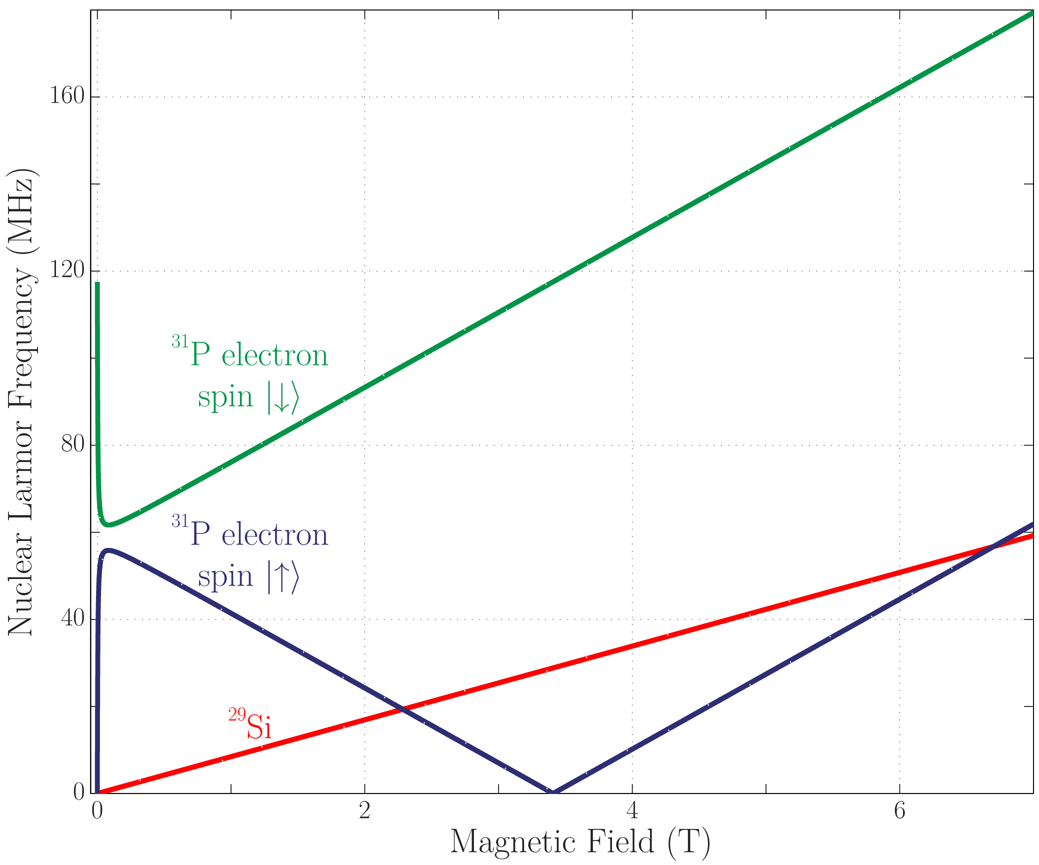

Figure 3.1: The Larmor frequencies of ^{29}Si and neutral ^{31}P nuclei. The nuclear Larmor frequency of the ^{31}P donor is dependent on the state of the donor electron, leading to two distinct Larmor frequencies possible for each D^0. In this figure, the curves labelled 'electron spin $|\updownarrow\rangle$' refer to the Larmor frequencies of the ^{31}P neutral donor nuclei that occur when the electron is either spin $|\uparrow\rangle$ or spin $|\downarrow\rangle$. Note that the energies of the $|\uparrow\Uparrow\rangle$ and $|\uparrow\Downarrow\rangle$ states cross at $\sim$3.4 T, and from that point on $E_{|\uparrow\Uparrow\rangle} < E_{|\uparrow\Downarrow\rangle}$.

^{31}P and ^{29}Si nuclear spin systems. This means that a ^{31}P-^{29}Si nuclear spin flip-flop conserves both energy and spin angular momentum ($\Delta E = E_f - E_i = 0$ and $\Delta M = 0$). This resonant matching condition creates a strong coupling between ^{31}P and ^{29}Si nuclei that is dependent on the state of the donor electron. Any spin polarization built up in the ^{31}P nuclei will couple to nearby ^{29}Si spins via a dipole-dipole interaction and diffuse away from the donors to the host nuclei in the same way that it diffuses from ^{29}Si to ^{29}Si, as explained in Section 2.4.1. However, since the coupling is dependent on the state of the donor electron, this coupling can be switched off by allowing the electron to relax into $|\downarrow\rangle$, ionizing the donor (moving to high temperature), or by changing B_0 from the resonant field. Now that we have identified this resonance condition, we must show that it actually facilitates polarization transfer from the ^{31}P nuclei to the ^{29}Si.

3.2 Nuclear Magnetic Resonance Detection Methods

To detect ^{29}Si polarization due to the transfer of spin magnetization from the ^{31}P , we must use a detection method that is sensitive to the polarization of a spin system. The ideal way to accomplish this is through a simple pulsed NMR detection scheme [72].

3.2.1 NMR in the Rotating Reference Frame

An individual nuclear spin i sitting in a magnetic field $\mathbf{B}_0$ will obey Larmor's theorem, which states the motion of the nuclear spin's magnetization vector $\mathbf{M}_i$ is governed by the equation [72]

$$\frac{\mathrm{d}\mathbf{M}_i}{\mathrm{d}t} = \mathbf{M}_i \times \gamma_I \mathbf{B}_0 \ . \tag{3.1}$$

This implies that if the spin is in an eigenstate of $\hat{I}_z$ (i.e. $\mathbf{M}_i$ is parallel or anti-parallel to $\mathbf{B}_0$) $\mathbf{M}_i$ will be time independent. However, if the spin is not in an eigenstate of $\hat{I}_z$ (i.e. $\mathbf{M}_i$ is not parallel or anti-parallel to $\mathbf{B}_0$), then one can see that $\mathbf{M}_i$ will precess about $\mathbf{B}_0$ at the Larmor frequency $\omega_I = \gamma_I B_0$ such that $|\mathbf{M}_i|$ is constant. One can simplify the description of this motion by a change of reference frame to one that is precessing about $\mathbf{B}_0$ at the Larmor frequency. We define the unit vectors of the rotating frame $\hat{x}' = \cos(\omega_I t)\hat{x}$, $\hat{y}' = \sin(\omega_I t)\hat{y}$, and $\hat{z}' = \hat{z}$. In this reference frame, $\mathbf{M}_i$ is stationary, regardless of its phase ϕ_I and the angle it makes with the z' axis θ_I.

To manipulate the magnetic moment of the spin, one can apply a radio-frequency (RF) electromagnetic field that is rotating in the x-y plane perpendicular to $\mathbf{B}_0$ in the stationary laboratory reference frame such that its frequency $\omega_{\mathrm{RF}} \approx \omega_I$. The Hamiltonian that describes the control field is given by [27]

$$\hat{H}_{\mathrm{RF}} = -\hbar\gamma_I B_1 \left[\hat{I}_x \cos(\omega_{\mathrm{RF}} t + \phi_{\mathrm{RF}}) - \hat{I}_y \sin(\omega_{\mathrm{RF}} t + \phi_{\mathrm{RF}})\right] \ , \tag{3.2}$$

where B_1 is the amplitude of the rotating control field and ϕ_{RF} is its phase. Assuming $\omega_{\mathrm{RF}} \approx \omega_I$, in the reference frame rotating at ω_I, $\mathbf{B}_1(t)$ will lose its time-dependence. By arbitrarily choosing $\phi_{\mathrm{RF}} = \frac{\pi}{2}$, $\mathbf{B}_1$ will be a vector with constant magnitude pointing along the y' axis in the rotating frame. In a manner similar to the precession of $\mathbf{M}_i$ about $\mathbf{B}_0$, Larmor's theorem dictates that the spin will begin to nutate about $\mathbf{B}_1$ in the x'-z' plane of the rotating frame with nutation frequency $\omega_1 = \gamma_I B_1$, as illustrated in Fig. 3.2.

By pulsing $\mathbf{B}_1(t)$ for a length of time t_p, one can stop the nutating magnetization at a specific angle $\theta_I = \gamma_I B_1 t_p$. After the pulse is turned off, the spin magnetization will undergo its usual precession in the laboratory frame due to $\mathbf{B}_0$ with constant θ_I and ϕ_I [72].

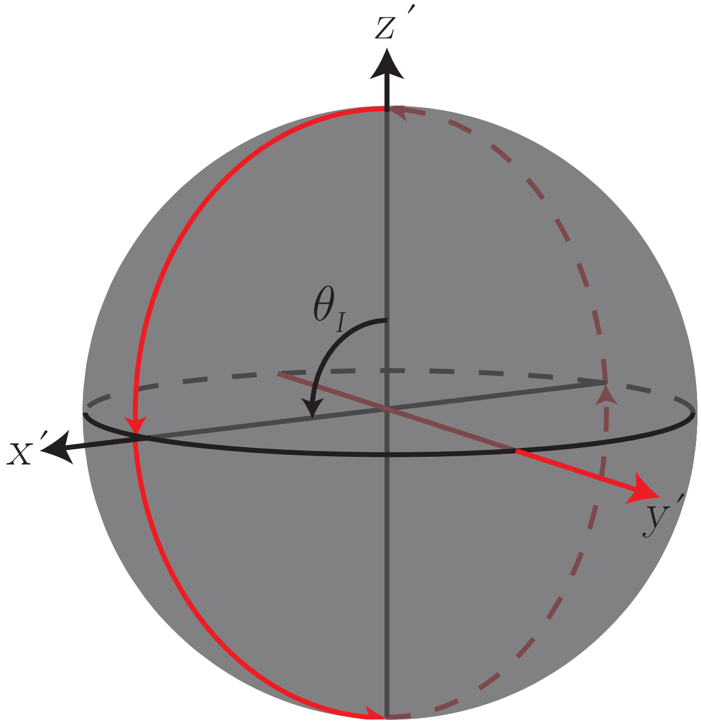

Figure 3.2: This illustration depicts the nutation of a nuclear spin in the rotating reference frame. $\mathbf{B}_0$ is oriented along the z' axis. The y' axis (in red) is the axis of nutation that the on-resonance RF field is oriented along. When in the presence of this on-resonance field, the spin magnetization will nutate in the x'-z' plane along the path indicated in red. An RF field pulsed for a length of time t_p rotates the spin an angle $\theta_I = \omega_1 t_p$. When the field is turned off, the spin will remain stationary in the rotating frame with constant θ_I and ϕ_I. Meanwhile, in the laboratory frame, the spin will undergo its usual Larmor precession due to B_0.

3.2.2 Experimental Pulsed NMR Detection

In practice, to perform an NMR experiment, the sample sits in an applied static magnetic field that lifts the degeneracy of the spin states and forces the spins to align parallel or anti-parallel to $\mathbf{B}_0 = B_0\hat{z}$ with the population of each state governed by the Boltzmann distribution at the given B_0 and temperature. To generate the rotating magnetic field, a cavity or coil (this thesis work uses a solenoid coil) that resonates at ω_I is placed around the sample with the axis of its RF magnetic field perpendicular to $\mathbf{B}_0$. The spin is then manipulated by applying a RF oscillating voltage in the coil with frequency $\omega_{\mathrm{RF}} \approx \omega_I$ that will generate a linearly oscillating magnetic field $\mathbf{B}_1(t)$ perpendicular to $\mathbf{B}_0$ in the laboratory frame. $\mathbf{B}_1(t)$ can be decomposed into two counter-rotating magnetic fields in the x-y plane perpendicular to $\mathbf{B}_0$. Since $\omega_{\mathrm{RF}} \approx \omega_I$, in the rotating reference frame one of the two counter-rotating components of the oscillating field will be stationary, while the other will be rotating in the opposite direction with a frequency of $\sim 2\omega_I$. Since this field will be so far off resonance, it will have a negligible effect on the nutation of the nuclear spin [72]. Hence, the spin will be subjected to the field described by the Hamiltonian in Eq. 3.2.

Now that the techniques of quantum control of the spin magnetization have been established, one must detect the signal that determines the ^{29}Si polarization. According to Faraday's Law of induction, a voltage $V(t)$ is induced in a coil of wire proportional to the rate of change of magnetic flux Φ_M through the coil $\left(\text{i.e. } V(t) \propto \frac{\mathrm{d}\Phi_M}{\mathrm{d}t}\right)$. For an ensemble of nuclear spins with a magnetization vector $\mathbf{M} = \Sigma_i \mathbf{M}_i$, $\frac{\mathrm{d}\Phi_M}{\mathrm{d}t}$ will be proportional to the rate of change of the transverse component of the ensemble's magnetization $\left(\frac{\mathrm{d}\mathbf{M}_{xy}(t)}{\mathrm{d}t} \propto \frac{\mathrm{d}\Phi_M}{\mathrm{d}t} \text{ where } \mathbf{M}_{xy} \text{ is the transverse component of the margnetization}\right)$. Since the time dependence of $\mathbf{M}_{xy}(t)$ is solely due to its precession about $\mathbf{B}_0$, we can write the flux $\Phi_M(t)$ due to the nuclear spin magnetization $\mathbf{M}$ through a N turn solenoid coil as

$$\Phi_M(t) = \mathbf{M} \cdot \mathbf{A} = M_{xy} A N \cos[\phi(t)] = M_{xy} A N \cos(\omega_I t + \phi_0) \ , \tag{3.3}$$

where A is the area of one loop of the coil and ϕ_0 is the phase of $\mathbf{M}$ when the oscillating voltage is initially detected. The z component of the magnetization of an ensemble of spin-$\frac{1}{2}$ nuclei with populations N_b and N_a is given by

$$M_z = \frac{1}{2}\hbar\gamma_I (N_b - N_a) \ , \tag{3.4}$$

implying that the induced nuclear polarization is

$$P_n = \frac{2}{\hbar\gamma_I (N_b + N_a)} M_z \ . \tag{3.5}$$

This implies that if the magnetization is tipped an angle θ_I away from the z axis by applying $\mathbf{B}_1(t)$, the transverse magnetization will be given by the projection of the resultant magnetization vector into the x-y plane. Assuming $|\mathbf{M}|$ is constant after the rotation by $\mathbf{B}_1(t)$, this projection is given by

$$M_{xy} = M_z \sin\theta_I = \frac{1}{2}\hbar\gamma_I(N_b + N_a)P_n \sin(\gamma_I B_1 t_p) \tag{3.6}$$

Given these assumptions,

$$\Phi_M(t) = \frac{1}{2}\hbar\gamma_I(N_b + N_a)AN\cos(\omega_I t + \phi_0)\sin(\gamma_I B_1 t_p)P_n \ , \tag{3.7}$$

implying $V \propto P_n$.

Hence, for a constant θ_I, one can determine P_n from the detected NMR signal solely by knowing the signal due to the equilibrium polarization. Furthermore, Eq. 3.7 implies that the maximum detected NMR signal will occur when $\theta_I = \frac{\pi}{2}$ and $\mathbf{M} = \mathbf{M}_{xy}$ [72]. This RF pulse that maximizes the induced NMR signal is referred to as a $\frac{\pi}{2}$ pulse.

Given an ideal system, once the nuclear spins have been rotated by applying $\mathbf{B}_1(t)$, the spins will relax into eigenstates of the system on a time scale that is given by its T_1 relaxation. However, local inhomogeneities in B_0 and different coupling strengths between nearby nuclear spins give rise to a slightly different effective magnetic field felt by each spin. This variation in effective field corresponds to a slightly different ω_I for each spin in the ensemble. The lack of uniformity in ω_I will cause the NMR signal to decay with a time scale T_2^*. For this reason, the signal detected in an NMR experiment is called a free induction decay (FID). Immediately after the spins are rotated, they are all in phase. However, due to the different ω_I values for each spin, instead of the ensemble's transverse magnetization being time independent in the rotating frame, some spins will precess faster and others slower and they will lose phase coherence. This manifests itself as an exponentially decaying envelope on the oscillating induced voltage, as seen in Fig. 3.3A. Over time, the net magnetization will become zero and no further voltage will be induced in the resonant coil.

We can use the FID signal intensity to determine the polarization of the nuclei in question. FID data from two of our ^{29}Si hyperpolarization experiments is shown in Fig. 3.3A. Taking the fast Fourier transform (FFT) of the FID gives an inhomogeneously broadened Lorentzian in frequency space, as seen in Fig. 3.3B. These Lorentzians are centred on the $\omega_{\mathrm{RF}} - \omega_I$, but in Fig. 3.3 they have been shifted so the results of the polarization procedure in two different temperature regimes can be compared more easily.

3.3 ^{31}P Hyperpolarization

In order to be able to effectively exploit the resonant spin polarization transfer process from the ^{31}P to nearby ^{29}Si, we must both hyperpolarize the donor nuclear spins and push the

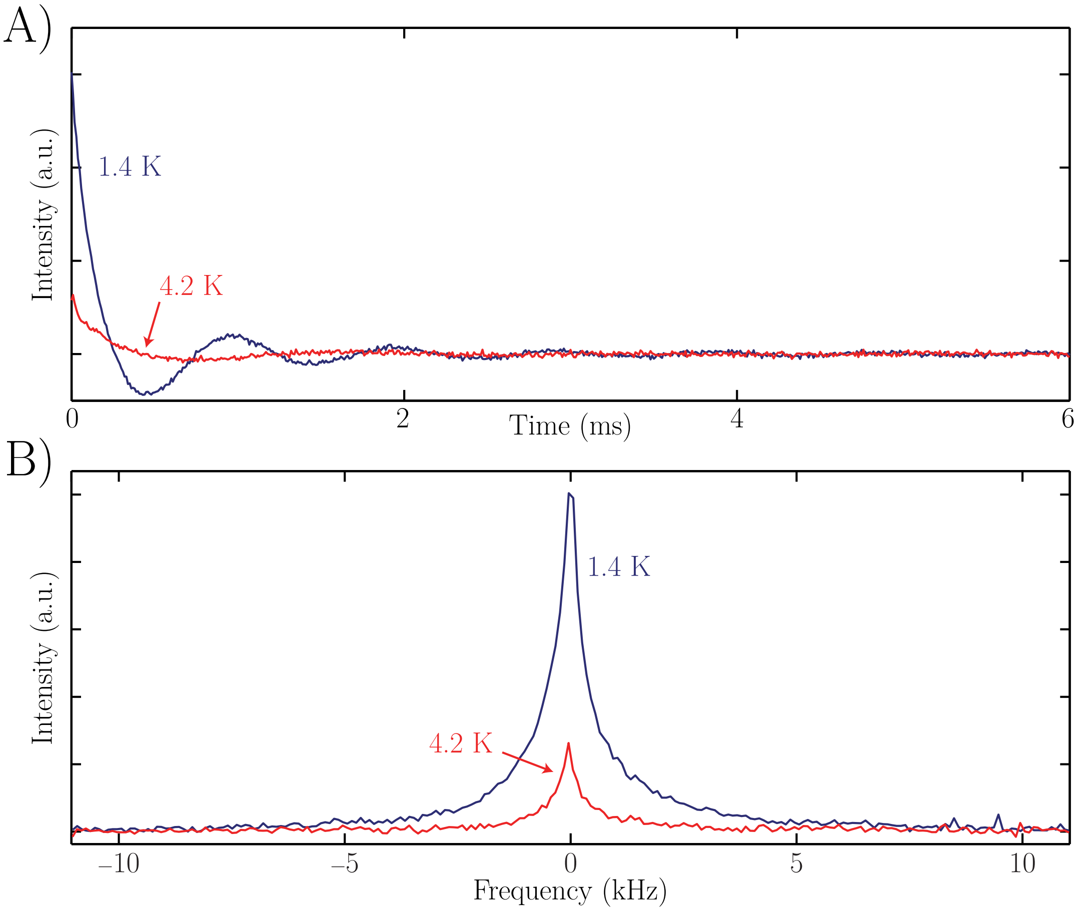

Figure 3.3: Examples of the ^{29}Si spectra after being polarized for 5 minutes at $\sim$2.2835 T at 1.4 K and 4.2 K. A) The FID signals detected by the NMR receiver due to the oscillating voltage induced in the resonant coil after an on-resonance $\frac{\pi}{2}$ pulse. The signal decay is due to the dephasing of the spin ensemble as it precesses in the transverse plane. B) The fast Fourier transform of the FIDs. The frequency scale is relative to the resonant RF frequency of $\sim$19.332 MHz used to generate the $\frac{\pi}{2}$ pulse. The two FFTs have been shifted by $\omega_{\mathrm{RF}} - \omega_{29}$ so the efficiency of hyperpolarizing the ^{29}Si in the two temperature regimes can be compared more easily. Note that the noise level in each temperature regime is approximately the same, implying a lower signal-to-noise ratio for experiments we ran at 4.2 K.

electrons of as many of the D^0 as possible into the spin $|\uparrow\rangle$ state . At low temperatures, there are a number of techniques that efficiently hyperpolarize dilute ^{31}P donor nuclei in Si. In isotopically enriched ^{28}Si, bound exciton optical methods are able to hyperpolarize the ^{31}P nuclear spins to $\gtrsim 90\%$ in under a second [73]. This is due to the D^0X lines being narrow enough to address and depopulate individual D^0 hyperfine spin states using single-frequency lasers [73]. In $^{\mathrm{nat}}$Si, broadband optical processes [64] and continuous wave (CW) electron spin resonance (ESR) techniques [55] that employ the nuclear Overhauser effect are made possible by the strong hyperfine interaction between the donor electron and nuclear spins.

At liquid He temperatures and at 2.2835 T, the optical linewidths of the resonant D^0X transitions are narrow enough in $^{\mathrm{nat}}$Si to selectively excite a particular electron spin state. Fig. 3.4 shows an illustration of how the ^{31}P hyperpolarization scheme we have proposed works. Starting from the equilibrium polarization in Fig. 3.4A, we resonantly create bound excitons in Fig. 3.4B conditional on them being in the electron spin $|\downarrow\rangle$ state by pumping bound exciton transitions 3 and 4, as labelled in Fig. 2.4A. Because the electrons in the bound exciton form a spin-singlet state, when it decays via Auger recombination it populates the conduction band with high spin temperature electrons. If the ionized donor is subsequently neutralized by a spin $|\uparrow\rangle$ electron, the donor moves out of optical resonance. Otherwise, an electron spin $|\downarrow\rangle$ neutralization event restarts the bound exciton creation and decay cycle until the donor is neutralized by a spin $|\uparrow\rangle$ electron, as illustrated in Fig. 3.4B. Over time, this effectively drives the donor electrons into the spin $|\uparrow\rangle$ state, creating a negative electron spin temperature and putting the donor nuclear spins in resonance with the surrounding ^{29}Si.

Since $T_{1\mathrm{e}}$ relaxation is mostly overpowered by resonantly pumping the D^0X transitions, inverting the donor electron spin states while operating at liquid helium temperatures creates a large negative electron spin temperature across the relaxation channel $T_{1\mathrm{x}}$ and drives an 'enhanced' NOE (see section 2.3.2 for details). As seen in Fig. 3.4C, this hyperpolarizes the ^{31}P into the $|\uparrow\Uparrow\rangle$ state, while at the same time putting the majority of the donor nuclei in resonance with the ^{29}Si.

3.4 Experimental Realization

We test the validity of this resonant hyperpolarization transfer process using an n-type $^{\mathrm{nat}}$Si sample with a ^{31}P doping concentration of $\sim 6 \times 10^{15}$ cm^{-3}. The sample was made up of four silicon pieces cut from the same wafer and stacked on top of each other. Each had dimensions of approximately 11 mm × 14 mm × 3 mm, giving an effective sample size of 11 mm × 14 mm × 12 mm. The sample is mounted in a home-built NMR probe that contains a variable capacitor. This capacitor allows us to adjust the resonant frequency of the coil to the ^{29}Si Larmor frequency while operating at different fields and temperatures.

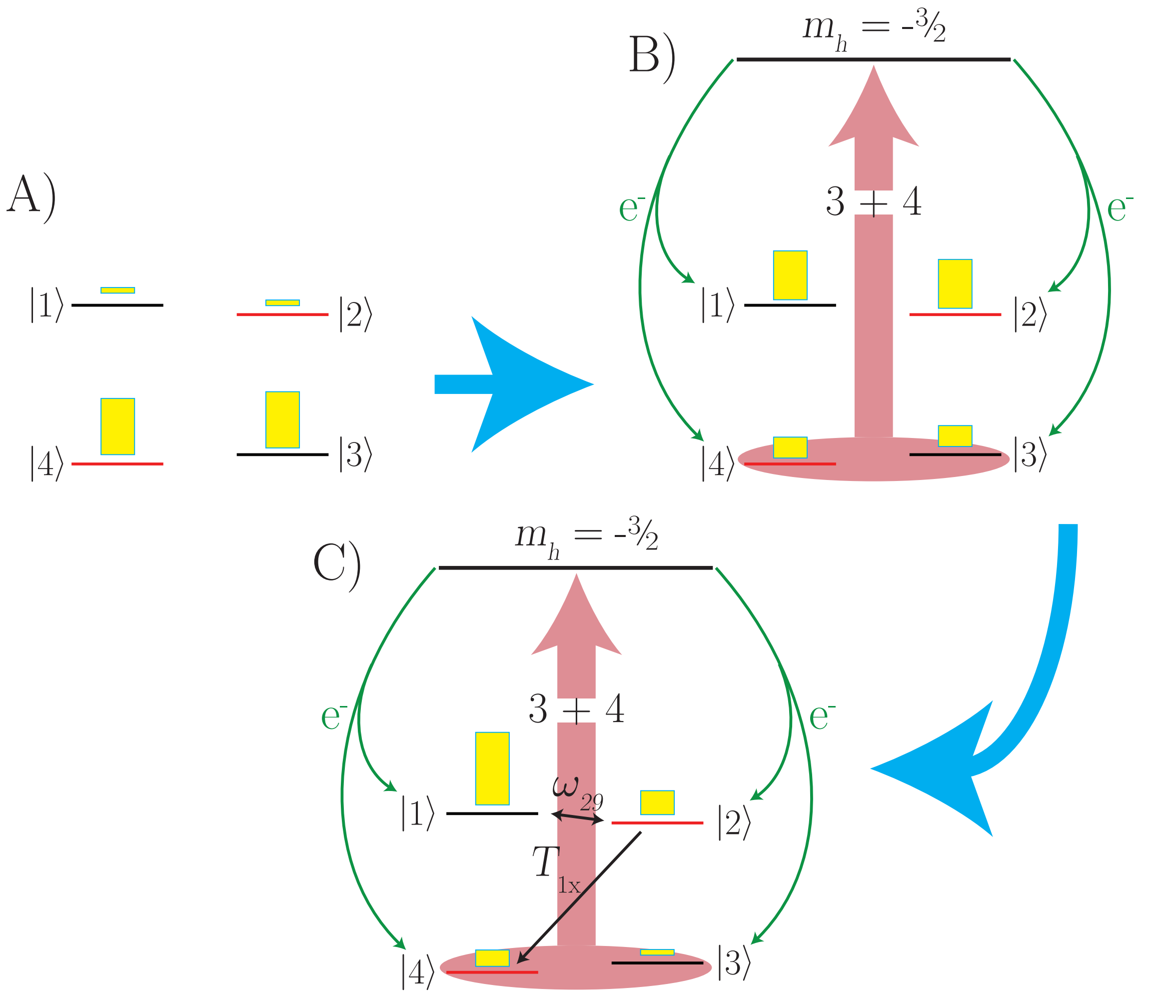

Figure 3.4: An illustration depicting the ^{31}P populations during the ^{29}Si polarization procedure. A) shows the the thermal polarization before the laser excitation. Shortly after the laser is turned on in B) the electron polarization changes as bound excitons are created and decay via Auger recombination prior to electron recapture by the donor. As the laser continues to polarize the donor electrons in C), $T_{1\mathrm{x}}$ cross relaxation drives a nuclear polarization that, when excited by the laser excitation, hyperpolarizes the donors into state $|1\rangle$. At 2.2835 T, $\Delta E_{12} = E_1 - E_2 = \omega_{29}$ and the hyperpolarization that has built up in state $|1\rangle$ diffuses to the nearby ^{29}Si centres via dipole-dipole mediated resonant spin flip-flops.

3.4.1 Cryostat and Magnet

The sample was inserted into a Janis Research Co. "SuperVaritemp" high homogeneity split-pair superconducting magnet cryostat with optical access that holds the liquid helium in a reservoir separate from the sample chamber [74]. The capillary tube connecting the two chambers can be closed, allowing us to run the experiment in different temperature regimes. To immerse the sample, we open the capillary tube and pull liquid helium into the sample chamber. We can then pump on the liquid helium vapour to operate at temperatures lower than 4.2 K. To operate at temperatures above 4.2 K, we first push the liquid helium in the sample chamber back into the reservoir. Then we turn on a heater at the opening of the capillary and flow a small amount of vaporized helium through it, allowing us to maintain a constant temperature above 4.2 K.

The cryostat contains a Janis Research Co. Superconducting Magnet System. This split-pair superconducting magnet is capable of operating at fields of up to 7 T with a homogeneity of ±0.01% over a 1 cm diameter at the centre of the field [74]. We were able to reproducibly set the magnetic field (with a precision of $\sim$0.02 mT) by using a high precision voltmeter to measure the voltage across a shunt resistor on the power supply. Using the relationship $B_0 = \frac{\omega_{29}}{\gamma_{29}}$, we were able to confirm the magnetic field we were operating at by monitoring the nuclear resonance frequency of the ^{29}Si. This allowed us to establish a linear relationship between the voltage drop across the shunt and ω_{29}. Hence, for experiments that required us to sweep B_0 we could adjust the field, tune the coil to ω_{29}, and set $\omega_{\mathrm{RF}} \approx \omega_{29}$ before the measurement. If we did not need to sweep B_0, then we could put the magnet into persistent current mode by disconnecting the power supply, allowing us to maintain a constant field for long periods of time.

We have two methods of determining the temperature when the sample is immersed in liquid helium. The first is monitoring the vapour pressure of the the liquid helium in the sample chamber. There is a well defined relationship between the vapour pressure and temperature of the liquid helium that gives us accurate readings of the temperature. This was facilitated by operating in only two liquid helium vapour pressure regimes: no pumping, corresponding to atmospheric pressure (4.2 K) and maximum pumping power, corresponding to 1-4 torr (1.4 ± 0.1 K). Additionally, we have a temperature sensor sitting at the bottom of the sample chamber near the opening of the capillary that connects the liquid helium reservoir to the sample chamber. This sensor is how we determine T when the sample is not immersed in liquid helium.

3.4.2 Optical Excitation

The laser excitation required (as discussed in Section 3.3) to drive D^{0}X transitions 3 and 4 was provided by a single frequency Koheras Adjustik ytterbium-doped fibre laser that will be referred to as the pump laser [75]. The frequency of the pump laser can be tuned with a temperature controller or by applying a voltage across a piezo-electric modulator. To polarize the ^{31}P, we centre its frequency on the ^{31}P bound exciton transitions 3 and 4 to throw the D^0 system out of equilibrium and allow the NOE to generate the nuclear hyperpolarization. Given that the bound exciton lines in $^{\mathrm{nat}}$Si are inhomogeneously broadened, we dither the laser frequency $\pm\sim 0.9$ GHz from the centre frequency (~ 1.8 GHz bandwidth) by applying a 3 Hz oscillating voltage across the piezo-electric modulator in the laser. This allows more of the ^{31}P neutral donors to be in optical resonance with the pump laser.

We are also able to excite electrons directly from the Si valence band to the conduction band using a neodymium doped yttrium lithium fluoride (Nd:YLF) laser that lases at a wavelength of 1047 nm, such that $\hbar\omega > E_g$. This type of excitation creates free electrons and holes. The electrons saturate the conduction band with approximately equal numbers possessing spin $|\uparrow\rangle$ and spin $|\downarrow\rangle$. If, upon recombination, the electrons are recaptured by ^{31}P donors, they will partially saturate the donor electron spin states. This will drive a 'standard' Overhauser process that will polarize the ^{31}P nuclei. The saturation factor s for this type of excitation will fall into the regime where $0 < s < 1$.

3.4.3 NMR Probe

The NMR probe used to deliver the resonant RF excitation to the sample is made up of a series-parallel tank circuit. The coil generating $\mathbf{B}_1(t)$ is a 20 turn rectangular coil wound with 0.25 mm diameter wire and 0.25 mm loop spacing. A 3.3 pF capacitor in parallel with the coil and a 1-10 pF in series sit in the tail of the cryostat. We can modify its capacitance by turning a glass rod attached to the capacitor that pokes out of the flange on the top of the sample chamber. Altering B_0 changes ω_{29} and varying the temperature changes the resonant frequency of the tank circuit. The variable capacitor allows us to keep the circuit's resonant frequency equal to ω_{29} so we can rotate the spin magnetization with consistent B_1. We built the probe at room temperature, and when we immersed it in liquid helium, the resonance of the circuit shifted too much for the variable capacitor to compensate. To bring the resonance of the circuit back to within range of adjustments of the variable capacitor, we added an additional 39 pF capacitor in series outside the dewar.

We impedance match, determine the resonant frequency, and find the bandwidth of the tank circuit using a Morris Instruments RF Sweeper. The bandwidth of the circuit at 19.314 MHz is ~ 200 kHz, implying a Q-factor of ~ 100.

3.4.4 NMR Detection

A diagram of the experimental set up used in this thesis to hyperpolarize the ^{31}P and detect spin diffusion to the ^{29}Si is given in Fig. 3.5. With the pump laser dithering about the centre frequency of D^{0}X lines 3 and 4 (details on how we determine this value in section 3.4.5), we illuminate the sample at liquid helium temperatures ($T \leq 4.2$ K) and allow the induced

^{31}P nuclear spin polarization to diffuse from the ^{31}P to the ^{29}Si centres. We stop the hyperpolarization process by closing a shutter and allowing a short period of time ($\sim$30 s) for the free carriers to be captured and the system to reach a steady state. After the system equilibrates, we then apply a $\frac{\pi}{2}$ pulse and detect the FID. After each FID we detect, we apply a long RF pulse ($\geq$ 5 ms) at the ^{29}Si resonant frequency to maximally mix the ^{29}Si polarization state, effectively setting the polarization to zero and erasing the history of previous polarization attempts.

A SpinCore RadioProcessor board generates the RF excitation required to rotate the ^{29}Si nuclear spins and detects the resultant FID [76]. The RF excitation is fed through a transmission amplifier that brings the power to $\sim$6 W. A 100 μs delay is inserted between when the RF pulse is applied and the FID is detected to eliminate the possibility of detecting the RF pulse as it rings in the resonant coil. After the delay, the resultant induced oscillating voltage is amplified by passing it through two Minicircuites preamplifiers before it is detected.

There are two parts to an NMR experiment: transmission and detection. Both of these must be taken into account when connecting the RF transmitter and receiver to the tank circuit. During transmission, it is necessary that as much power as possible is incident on the tank circuit and that the excitation pulse does not damage the delicate preamplifiers that are necessary to detect the FID. During detection, the objective is to allow as much of the FID signal as possible into the detector, while protecting the signal from the noise due to the transmission amplifier. To do this, we use a $\frac{\lambda}{4}$ cable and two sets of crossed diodes to create a transmit/receive switch (T/R), as seen in Fig. 3.5. Due to a diode's nonlinear impedance-voltage relation, an individual set of crossed diodes will act like switches that will be closed for large signals and open for small signals [72].

To protect the preamplifiers during transmission, we have placed a set of crossed diodes D_2 connected to ground just before the input to the receiver. This will short out any of the high powered excitation pulse that could damage the preamplifiers in the receiver. However, we also want as much of the excitation pulse as possible to be incident on the tank circuit. To that effect, we cut the coaxial cable between the two sets of diodes D_1 and D_2 to be a quarter wavelength $\left(\frac{\lambda}{4}\right)$ of the $\sim$ 19.3 MHz excitation pulse. When the RF excitation pulse is transmitted, the diode switch will be closed and the voltage at D_2 will be held at zero. Because the $\frac{\lambda}{4}$ coaxial cable is not terminated at 50 Ω, the excitation pulse will be reflected back and will create a standing wave of current and voltage in the $\frac{\lambda}{4}$ line. The impedance at any point in the $\frac{\lambda}{4}$ cable will be given by $Z = \frac{V}{I}$, where V is the voltage and I is the current. At D_1, the voltage will be maximum and the current will be minimum. This results in maximum Z and minimal RF power diverted from the NMR probe [77].

To protect the NMR signal from noise due to the powerful transmission amplifier, we have placed a diode switch D_1 on the output of the RF pulse transmitter. This will allow the high powered excitation pulse to pass while shielding the receiver from the amplifier

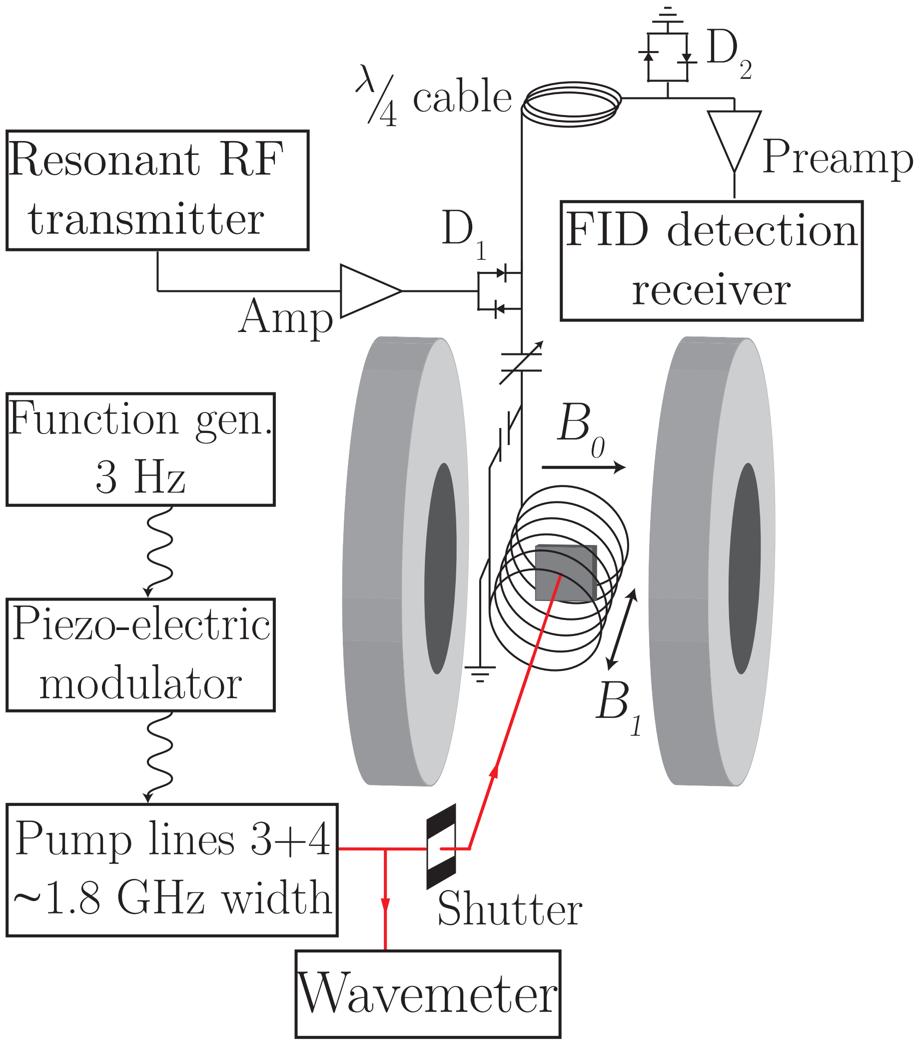

Figure 3.5: This diagram illustrates the set up used to hyperpolarize the ^{29}Si and subsequently detect its FID. Using a tunable capacitor, the resonant frequency of the tank circuit is centred on the ^{29}Si resonant frequency. The polarizing pump laser frequency is set to the centre of D^0X transitions 3 and 4. Due to inhomogeneous broadening of the D^0X transitions in $^{\mathrm{nat}}$Si, we apply a 3 Hz oscillating voltage from a signal generator to the piezo-electric modulator in the pump laser to dither its frequency over a ~ 1.8 GHz bandwidth. This puts as many of the ^{31}P nuclei in optical resonance as possible, increasing the ^{31}P hyperpolarization. When the laser has finished polarizing the sample, a shutter is closed and after 30 s the SpinCore RadioProcessor NMR board sends a $\frac{\pi}{2}$ pulse to the sample and detects the resultant FID. The two sets of crossed diodes (D_1 and D_2) combined with the $\frac{\lambda}{4}$ coaxial cable act like a transmit/receive switch. When it is in transmission mode the setup allows the transmitted RF pulse to rotate the spin magnetization with maximum power without losses through D_2. This implementation also prevents the excitation pulse from damaging the delicate preamplifiers in the receiver. Then, while in receiving mode, the induced voltage will be detected by the FID receiver while any noise from the transmission amplifier will excluded. Figure is adapted from [50].

noise, which will not have a high enough voltage to forward bias the diodes. Similarly, the induced oscillating voltage has an amplitude much too small to forward bias any of the diodes and both diode switches appear to be open. Hence, we are able to collect the full NMR signal without losses.

When we vary the temperature of the sample, the probe's resonant frequency changes. Similarly, when the static magnetic field is varied, the ^{29}Si resonant frequency changes. To that effect, we have built the resonant circuit with a tunable capacitor that allows us to match the resonant frequency of the coil to that of the ^{29}Si, allowing us to excite the RF transitions with consistent B_1.

3.4.5 Photoconductive Spectrum

To determine the optimal frequency for the hyperpolarizing laser excitation, we use a variant of the spectroscopic technique photoluminescent excitation (PLE) to find the frequencies of the D^{0}X transitions. This technique differs from typical PLE experiments because instead of detecting the optical resonances by monitoring photon emission, we detect changes in the resistivity of the material due to photoconductivity: a change in the conductivity of the sample due to photon absorption.

When laser excitation resonantly creates a bound exciton (see Fig. 2.4 for an illustration of the D^{0}X state) and it decays via Auger recombination, an electron is kicked into the conduction band, lowering the resistivity of the semiconductor. The experimental setup used to detect the photoconductivity due to these excitation and decay cycles is illustrated in Fig. 3.6.

We determine the ^{31}P D^{0}X spectrum by locking the pump laser to the external cavity described in [43] and scanning it across the transition frequencies of the ^{31}P D^{0}X lines. To detect changes in the conductivity, we use a technique similar to ‘contactless electrically detected magnetic resonance’ readout [78, 50]. The sample is mounted in the previously described NMR probe and is immersed in liquid helium. We apply a 19.3 MHz CW RF voltage to the coil, which is tuned to produce minimum reflected power at that frequency (matched), and monitor the power of the reflected signal using a directional coupler and a power sensor that outputs a proportional voltage. This voltage is detected and plotted against the energy of the laser, monitored by a wavemeter. When the laser comes into resonance with one of the D^{0}X transitions and increases the number of free carriers, the oscillating magnetic field causes these carriers to generate eddy currents in the material and absorb some of the RF power, increasing the amount that is reflected back. This is equivalent to a change in the matching of the coil and allows us to detect the energies of the D^{0}X transitions we will pump to hyperpolarize the ^{29}Si.

Fig. 3.7 shows a spectrum of the six lowest energy ^{31}P bound exciton optical transitions (labelled 1-6 in Fig. 2.4) at 4.2 K and the resonant 2.2835 T field that will be used to hyperpolarize the ^{29}Si centres. The width of the D^{0}X lines we will pump to hyperpolarize

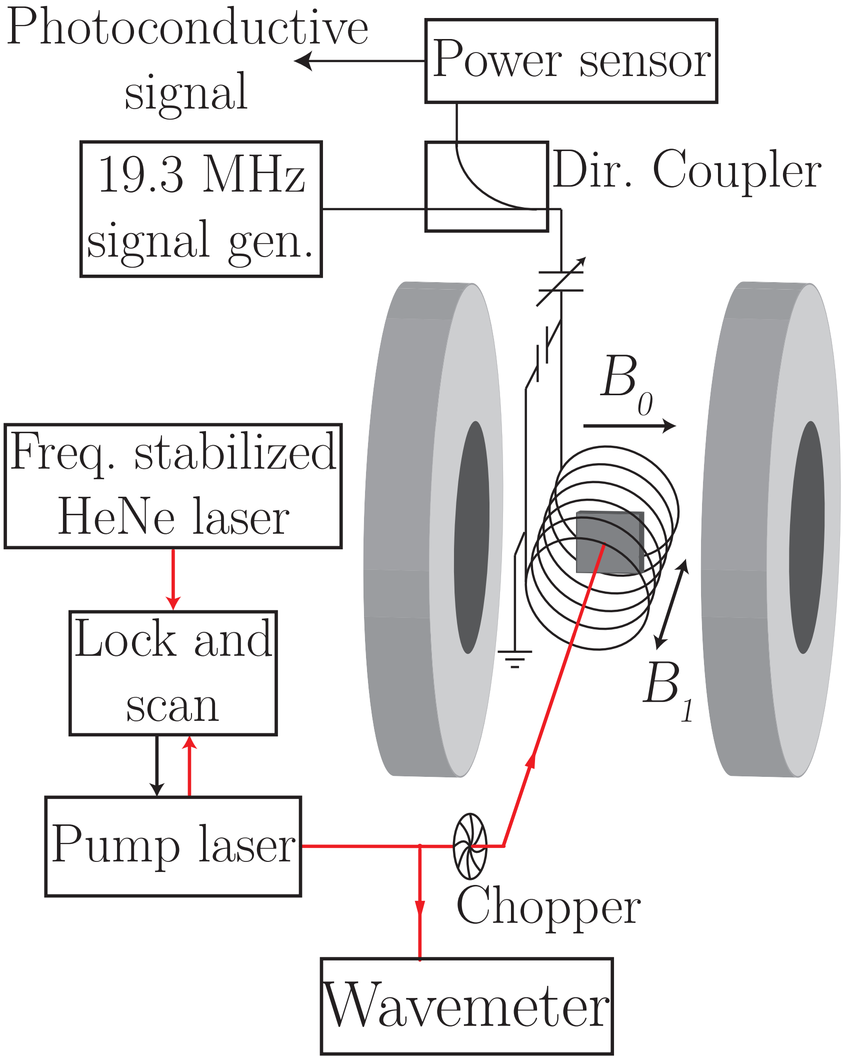

Figure 3.6: An illustration of the experimental setup used to detect the photconductive spectrum of the D^0X transitions. The sample is immersed in liquid helium and is mounted in the NMR probe used to detect the polarization of the ^{29}Si nuclei. The pump laser (also the laser used to hyperpolarize the ^{29}Si) is frequency locked to a cavity using a stabilized HeNe laser as a reference. We step the frequency of the pump laser, allowing us to scan it over the region of interest and monitor this frequency with a wavemeter. As the laser scans over the D^0X transitions, we look for corresponding changes in the photoconductivity of the sample. We detect these by driving an oscillating voltage in the NMR coil and looking for changes in the power of the reflected signal fed through a directional coupler to a power sensor. Figure is adapted from [50].

the ^{29}Si (lines 3 and 4) is ~ 2.5 GHz. This implies that the ~ 1.8 GHz bandwidth of the dithered polarizing excitation will not be able to generate bound excitons for all the ^{31}P donor centres, leaving the donors that fall within the tails of the line out of optical resonance.

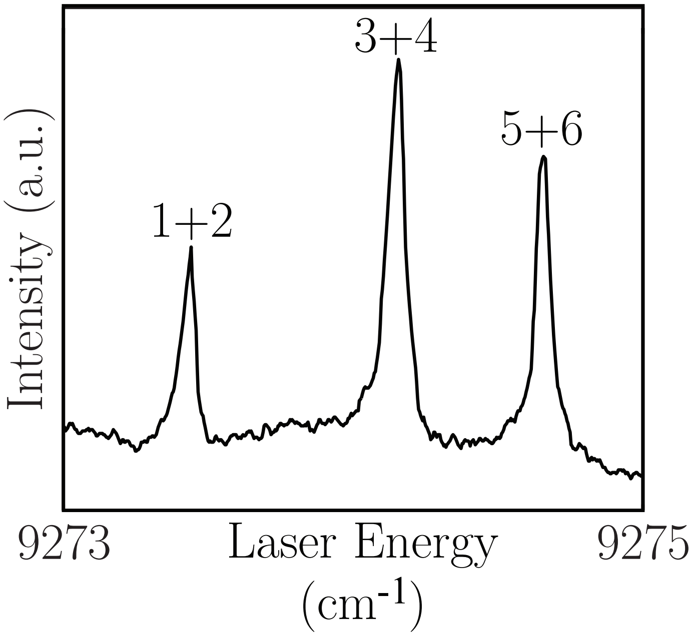

Figure 3.7: A photoconductive spectrum of D^{0}X transitions 1-6 at 2.2835 T and 4.2 K. The labels 1+2, 3+4, and 5+6 refer to the D^{0}Xtransitions as labelled in Fig. 2.4A. From this spectrum the pump laser could be accurately set to the centre of the 3+4 D^{0}X transition.

3.4.6 Rabi Cycle

When the on resonance RF control pulse is applied to the spin magnetization vector, it nutates about $\mathbf{B}_1$ in the rotating reference frame (see section 3.2.1 for details and Fig. 3.2 for an illustration of this). Because the size of the FID signal is due to the projection of the precessing magnetization into the x-y plane, to maximize the FID, we must first determine the proper length of the $\frac{\pi}{2}$ pulse $\left(\text{when } \theta_I = \frac{\pi}{2}\right)$.

We can determine this pulse length by looking at the oscillations due to a Rabi cycle. In a Rabi cycle experiment (detailed in Fig. 3.8), we first polarize the nuclear spins in the sample and then apply RF control pulses of varying duration and observe how the NMR signal depends on the pulse length. The projection of the magnetization into the transverse plane (and hence, the signal magnitude) is proportional to $\sin^2(t_p\omega_1)$, where t_p is the pulse length and $\omega_1 = \gamma_I B_1$ is the nutation frequency.

The data we have collected that allows us to determine the $\frac{\pi}{2}$ pulse length of our system of ^{29}Si spins is shown in Fig. 3.9. Once we collected the data from the Rabi experiment, we fit the first peak to the function $A\sin^2(\omega_1 t_p) + C$, where the amplitude A, nutation frequency ω_1, and vertical offset C were the free parameters. From this fit, we were able to determine $\omega_1 = 32 \pm 2$ kHz implying that the length of the $\frac{\pi}{2}$ pulse $t_{\frac{\pi}{2}} = \frac{\pi}{2\omega_1} = 49 \pm 3$ μs. This $\frac{\pi}{2}$ pulse length was used throughout the rest experiment.

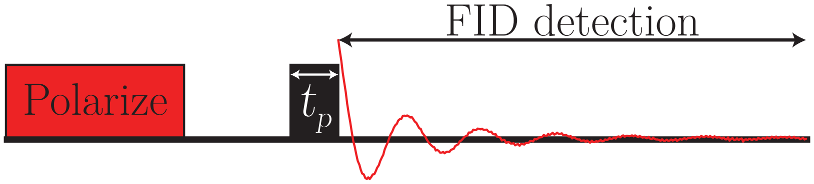

Figure 3.8: This diagram illustrates the steps of the Rabi cycle experiment used to determine the correct $\frac{\pi}{2}$ pulse length. First the spins are polarized, then a resonant RF pulse is applied to the spins, and the FID is detected. The duration of the RF pulse (t_p) is varied and the first maximum in the in the plot of signal intensity versus t_p determines the correct $\frac{\pi}{2}$ pulse length $t_{\pi/2}$.

3.4.7 The Experimental Parameters

Now that we have found $t_{\pi/2}$, we can determine the efficiency of this all-optical polarization scheme, look at the mechanisms behind the ^{29}Si hyperpolarization, and attempt to understand the limiting factors in the polarization rate. Central to this hyperpolarization method is the effect that B_0 mediated resonant hyperpolarization transfer from ^{31}P to ^{29}Si nuclei has on the polarization rate. We are able to determine the magnitude of this effect by varying the applied magnetic field slightly from the ^{31}P-^{29}Si resonance condition and detecting the polarization at each magnetic field.

Once we have established the principle of resonant spin diffusion from the ^{31}P donors to ^{29}Si nuclei, we can vary parameters like the temperature, excitation conditions (pump laser frequency and power), and the exposure time. Finally, to determine the actual fraction of the ^{29}Si nuclei we have successfully hyperpolarized, we must determine the equilibrium polarization signal by allowing unpolarized ^{29}Si nuclei to equilibrate to the thermal polarization. However, the extremely long ^{29}Si T_1 that is so important for its various applications makes this parameter difficult to directly determine at liquid helium temperatures. We were therefore required to exploit several temperature dependent processes to arrive at a value for the equilibrium ^{29}Si NMR signal.

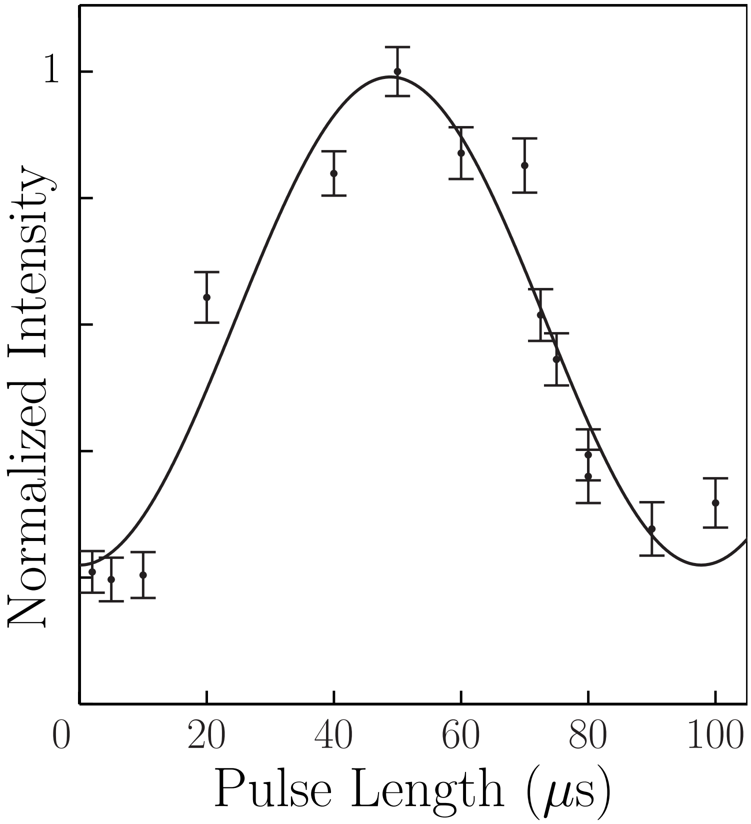

Figure 3.9: The Rabi cycle data taken at 4.2 K with a polarization time of of 3 minutes for each data point. The data is normalized to the maximum value. Error bars are determined from the noise level of the signal intensity and the function $A\sin^2(\omega_1 t_p) + C$ was fit to the the data. The amplitude of the oscillations A, nutation frequency ω_1, and offset C were left as fit parameters. The nutation frequency determined from the fit is 32 ± 2 kHz implying that the $\frac{\pi}{2}$ pulse length is 49 ± 3 μs. A detailed survey of t_p was only performed up through 100μs.

Chapter 4

Results and Discussion

Section 3.4.7 outlined the important experimental parameters we must consider in this project. In this chapter, we will present the results of varying said parameters and the effects that changing the conditions used to polarize the ^{29}Si have on the efficiency of this procedure. By understanding these effects, we will be able to make inferences about the dynamics of this polarization scheme as well as present ways to potentially improve this technique. First, we will examine the effect of polarizing the ^{29}Si at the resonant matching field under two temperature regimes. Then, we will explore what varying the frequency and intensity of the laser excitation used to hyperpolarize the ^{31}P can tell us about the mechanisms at work in the sample during this procedure. Finally, we will determine the ^{29}Si NMR signal that corresponds to the thermal Boltzmann polarization, observe how the ^{29}Si hyperpolarization signal depends on the duration of the optical excitation, and ultimately determine the fraction of the ^{29}Si nuclei we were able to hyperpolarize in the longest polarization time investigated, 64 hours.

4.1 Resonant Spin Transfer

Before moving forward with this project, we needed to confirm that resonantly transferring spin hyperpolarization from ^{31}P nuclei to the ^{29}Si was an effective method of generating a highly polarized ensemble of nuclei in our sample. The Larmor frequency matched resonance condition between the donor nuclei with electron spin $|\uparrow\rangle$ and the ^{29}Si is dependent on B_0.

Therefore, we can observe how the ^{29}Si polarization depends on B_0 in the region surrounding 2.2835 T and determine whether the dependence suggests that resonant transfer of polarization between the ^{31}P and ^{29}Si is occurring. To do this, we first tune the NMR probe to the ^{29}Si resonance frequency at a range of static magnetic fields about 2.2835 T and then directly detect the ^{29}Si NMR signal after 5 minutes of hyperpolarization at each point.

We first examined this resonant transfer process at 4.2 K, but unfortunately operating at the resonant field only improved the ^{29}Si polarization by approximately a factor of two, as seen in Fig. 4.1. However, we can see in Fig. 4.1 that when pumping on the liquid helium vapour to lower the temperature to 1.4 K, we were able to improve the ^{29}Si polarization by approximately an order of magnitude when operating at the resonant matching condition. We also find that the resonance condition did not occur at the exact magnetic field and ^{29}Si frequency we were expecting (2.2835 T and 19.314 MHz). The maximum value of the data in Fig. 4.1 occurs at 2.2857 T with a ^{29}Si resonant frequency of 19.332 MHz and a ^{31}P resonant frequency of 19.277 MHz. The cause of this will be discussed in section 4.1.2.

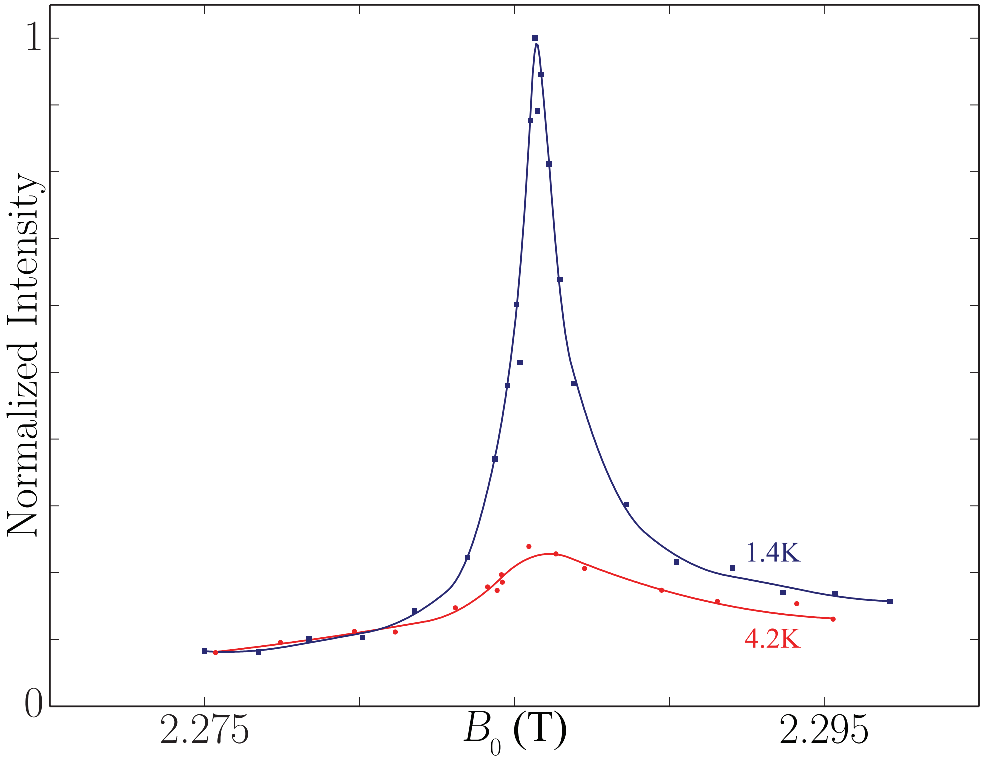

Figure 4.1: The magnetic field and temperature dependence of the ^{29}Si polarization when illuminated for 5 minutes. The magnetic field was determined using the relation $B_0 = \frac{\omega_{29}}{|\gamma_{29}|}$, with $\gamma_{29} = -8.458$ MHz$\cdot$mT^{-1} [66]. The data is normalized to the maximum value achieved at 1.4 K. The signal error is the size of the data points and the spline fits are solely a guide for the eye.

4.1.1 Temperature Dependence

Temperature affects several parameters that contribute to the dramatic improvement we see when polarizing at 2.2857 T and 1.4 K. At pumped liquid helium temperatures, the equilibrium polarization of the donor electron is ~ 0.80 as compared to ~ 0.35 at 4.2 K (a factor of ~ 2.3). Recalling Eq. 2.10, due to the principle of detailed balance we expect to see an improvement in the ^{31}P polarization rate due to a decrease in temperature given by $\exp\left[\frac{\Delta E}{k_B}\left(\frac{1}{T_L} - \frac{1}{T_H}\right)\right]$. In this case, $\Delta E \approx 63.879$ GHz, $T_L = 1.4$ K, and $T_H = 4.2$ K. This implies that the ratio $R_{2\to4}/R_{4\to2}$ increases by a factor of $\sim$4.3. This accounts for nearly all of the five-fold improvement in the ^{29}Si hyperpolarization rate at the matching field by moving to a lower temperature. Additional improvement in the ^{29}Si hyperpolarization rate can also be attributed to the donor electron T_1 increasing when moving from 4.2 K to operate at 1.4 K [55]. By increasing $T_{1\mathrm{e}}$, the saturation factor increases and we are able to generate a larger steady state donor electron spin inversion. This will keep more ^{31}P in resonance with the nearby ^{29}Si and drive a stronger NOE.

4.1.2 Width and Shape

The linewidth and asymmetry we observe on the high field tail of the ^{31}P-^{29}Si resonant transfer peak in Fig. 4.1 are due to the distribution of ^{29}Si nuclei about the ^{31}P donors. The asymmetry we see is not a hysteresis effect as it is independent of magnetic field sampling order. This implies it must be due to a shift in the resonant matching condition. This shift is a function of the small anisotropic hyperfine interaction present between the spin $|\uparrow\rangle$ donor electrons and the nearby ^{29}Si nuclei [29]. We can qualitatively confirm this by considering the effective ^{29}Si oscillation frequency [79]

$$\omega_{29}(\mathbf{r}_k, m_s) = \frac{1}{\hbar}\sqrt{(m_s A_{zz}(\mathbf{r}_k) - \underbrace{\gamma_{\mathrm{Si}}\hbar B_0}_{\text{unperturbed } ^{29}\text{Si Zeeman splitting}})^2 + m_s^2(A_{zx}^2(\mathbf{r}_k) + A_{zy}(\mathbf{r}_k))} \tag{4.1}$$

at lattice site k with position $\mathbf{r}_k$ relative to the location of the nearby neutral ^{31}P donor. $A_{zz}(\mathbf{r}_k)$, $A_{zx}(\mathbf{r}_k)$, and $A_{zy}(\mathbf{r}_k)$ are components of the hyperfine tensor $\mathbf{A}_k$ that can be split into isotropic (a_k) and anisotropic ($\mathbf{B}_k$) components such that $\mathbf{A}_k = a_k\mathbb{1} + \mathbf{B}_k$ [66, 79]. This spread of ^{29}Si Larmor frequencies distributed about the ^{31}P donors gives rise to the width of the resonant transfer peak. For the majority of the anisotropic hyperfine interactions that have been measured, the $A_{zz}(\mathbf{r}_k)$ term is orders of magnitude larger than $A_{zx}(\mathbf{r}_k)$ and $A_{zy}(\mathbf{r}_k)$ and for the resonant matching condition to apply, $m_S = +\frac{1}{2}$. Hence, there exists a characteristic downward shift of ω_{29} for ^{29}Si nuclei located in specific shells surrounding the donor [66, 42]. Since resonant spin transfer is conditional on the donor electron being spin $|\uparrow\rangle$, this downward shift in ω_{29} will alter the magnetic field resonant transfer is most effective at. B_0 will need to be slightly higher, as depicted in Fig. 4.2.

The transition probability W_{if} of a spin flip-flop between two interacting nuclei is dependent on the initial and final states of the unperturbed two particle Hamiltonian. According to Eq. 2.13, any $\Delta E_{if} \neq 0$ will decrease the transition probability per unit time. Hence, this will spoil the resonant matching condition for the ^{29}Si nearest the phosphorus donors and will have a negative effect on the rate of spin diffusion away from the ^{31}P. This problem has been well documented in the literature and is referred to as a spin diffusion barrier [5, 70, 80].

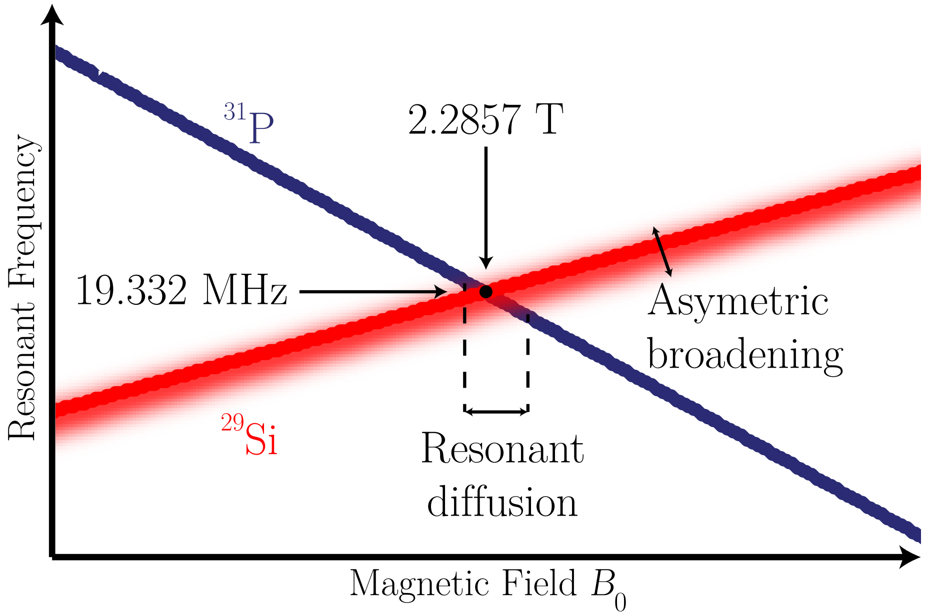

Figure 4.2: A diagram depicting the implications of the anisotropic hyperfine interaction between the donor electron and the ^{29}Si. This interaction shifts ω_{29} for the nuclei near the donors and leads to the asymmetric peak shape we see on the high field tail of Fig. 4.1.

This barrier of radius d was defined by Bloembergen [5] to be the distance from the impurity (in this case the ^{31}P donor) that the Larmor frequencies of two hyperfine-shifted neighboring spins is equal to the NMR linewidth [70]. Since the gradient in Larmor frequency is large for $\mathbf{r}_k < d$, we will need to polarize the ^{29}Si that lie outside the diffusion barrier in order for this hyperpolarization to readily diffuse into the bulk ^{29}Si. In our situation,it is possible the problem with the diffusion barrier could be mitigated by dithering B_0 while hyperpolarizing the ^{29}Si nuclei in an attempt to match the Larmor frequencies of as many of the ^{29}Si to those of the ^{31}P nuclei.

4.2 Variation of Optical Excitation Conditions

There are several parameters relating to the laser excitation conditions we can vary. The most illuminating, in reference to the dynamics of the polarization procedure we are employing, is the dependence of its effectiveness on the laser excitation frequency. By varying the frequency of the polarizing excitation, we can create negative, hot, or cold donor electron spin temperatures that generate enhanced, standard, or inverted ^{31}P Overhauser hyperpolarization.

4.2.1 Negative Spin Temperature

Up until now in this work, we have discussed the ^{29}Si polarization only under the conditions that we create a negative electron spin temperature. As seen in Fig. 4.3, the most effective method for hyperpolarizing the ^{29}Si is by creating a negative donor electron spin temperature. As we have done in the rest of this thesis, we pump D^0X transitions 3 and 4 (labelled 3+4) to drive an enhanced ^{31}P nuclear hyperpolarization. In addition to driving an enhanced NOE, pumping lines 3 and 4 puts the maximum number of ^{31}P nuclei in resonance with the ^{29}Si, allowing for the hyperpolarization to be diffused away from the ^{31}P most efficiently.

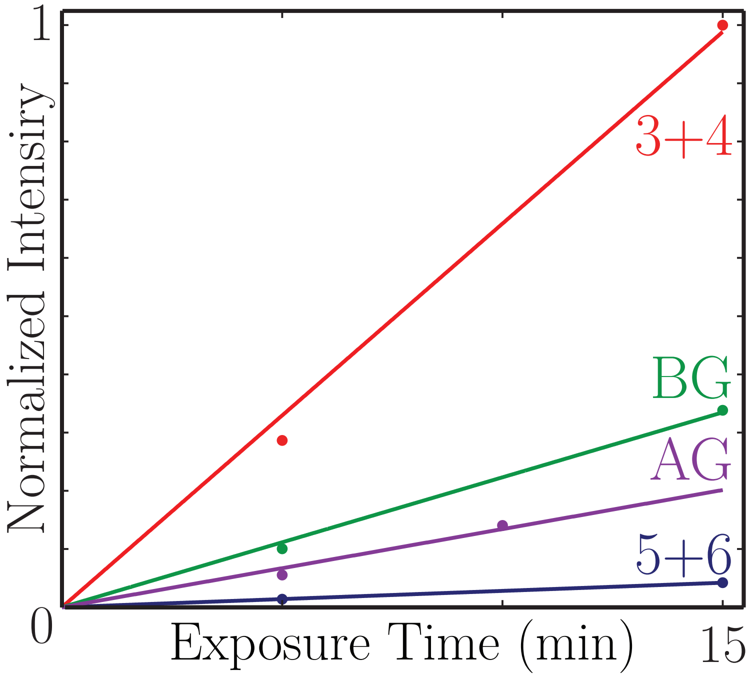

Figure 4.3: Here we compare the signal intensity of the ^{29}Si polarization under four different laser energy regimes at 2.2857 T and 1.4 K. The label 3+4 in the figure corresponds to the ^{29}Si polarization when driving D^0X transitions 3 and 4 with the Koheras fibre laser. The label 5+6 in the figure corresponds to the ^{29}Si polarization when driving D^0X transitions 5 and 6 with the Koheras fibre laser. The label BG corresponds to the ^{29}Si polarization when non-resonantly ionizing neutral donors with below bandgap excitation supplied by the Koheras fibre laser at an energy of ∼9275.08 cm^{-1}. The label AG corresponds to the ^{29}Si polarization when illuminating the sample with above bandgap laser excitation supplied by the Nd:YLF laser at ∼9551 cm^{-1}. The data is normalized to the maximum value.

4.2.2 Hot Spin Temperature

In contrast, we are able to create a hot electron spin temperature and drive a standard NOE by ionizing the donor electrons either with below-bandgap or above-bandgap nonresonant laser excitation (labelled BG and AG, respectively, in Fig. 4.3). BG excitation is supplied by the Koheras Yb-fibre laser emitting ~ 9275.08 cm^{-1} energy light, while AG excitation is supplied by a 1047 nm solid state laser (1047 nm $\approx$ 9551 cm^{-1}). These types of excitation create hot conduction band electrons that can neutralize ionized donors and partially saturate the donor electron spin states. BG excitation creates hot conduction band electrons by nonresonantly ionizing neutral donors, while AG excitation populates the conduction band by exciting electrons directly from the Si valence band. One must keep in mind that the BG nonresonant excitation is always present, even when we are resonantly driving the bound exciton transitions.

4.2.3 Cold Spin Temperature

By resonantly driving D^{0}X transitions 5 and 6, we are able to push what little thermal donor electron $|\uparrow\rangle$ population there is into the electron $|\downarrow\rangle$ state, creating a colder electron spin temperature. In principle, when we move donor electrons out of equilibrium from $|\uparrow\rangle$ to $|\downarrow\rangle$, we are driving a ^{31}P nuclear hyperpolarization into the opposite spin state as the excitation conditions that have been previously mentioned (3+4, BG, and AG in Fig. 4.3). Under this pumping regime, we are also removing the ability for the few donor nuclei that would be in resonance with the ^{29}Si to diffuse away any ^{31}P hyperpolarization we have created. However, because in thermal equilibrium at 1.4 K and 2.2857 T, the electron polarization is already ~ 0.80 spin $|\downarrow\rangle$, the laser is only able to resonantly create a very small number of bound excitons, leading to an extremely weak NOE that must compete against the ever present non-resonant BG excitation that drives a standard NOE. Hence, resonantly pumping lines 5 and 6 is not efficient enough to polarize the ^{29}Si into the opposite nuclear spin state. Even though polarizing the donor electrons into $|\downarrow\rangle$ generates an extremely weak NOE, this sheds light on the importance of not neglecting non-resonant BG ionization when we are resonantly pumping D^{0}X transitions 3 and 4. This non-resonant excitation has the possibility of compromising the maximum ^{31}P hyperpolarization we are able to achieve by reducing the the steady state donor electron population inversion.

4.2.4 Insights into the ^{31}P -^{29}Si Polarization Mechanism

The ^{29}Si polarization build up is more efficient at the resonant matching condition when resonantly pumping D^{0}X transitions 3 and 4 as well as when pumping with above-bandgap light (AG). This indicates that the NOE must hyperpolarize the ^{31}P nuclei first before the magnetization can diffuse out to the ^{29}Si. Any direct hyperpolarization from the non-equilibrium donor electron spins will occur much more slowly in this system due to the large difference in Larmor frequencies and weak coupling between the two spin systems [81]. Even though the laser intensity is slightly different when under nonresonant BG and AG excitation conditions (~ 220 mW$\cdot$cm^{-2} for BG and ~ 185 mW$\cdot$cm^{-2} for AG), the ^{29}Si hyperpolarization rates are similar (a factor of ~1.7). AG excitation will generate significantly more carriers and populate the conduction band much more efficiently with electrons excited directly from the valence band than BG excitation. Hence, we can say that the ^{29}Si hyperpolarization under nonresonant conditions does not significantly depend on the number of conduction electrons. The above observations rule out the possibility that the spin diffusion mechanism from the ^{31}P to the ^{29}Si is due to a conduction electron mediated nuclear spin coupling that could arise, for instance, from the Ruderman-Kittel-Kasuya-Yosida (RKKY) interaction [82].

4.2.5 Optical Intensity Dependence

As one might expect, the speed of this ^{29}Si hyperpolarization procedure is dependent on the intensity of the laser light incident on the sample. In Fig. 4.4, we can see that for low laser intensities (shown here < 250 mW·cm^{-2}) and a fixed ^{29}Si polarization time of 5 minutes, the polarization achieved is nearly linearly dependent upon the excitation intensity. However, we can see by fitting an exponential to the data, that at some point this trend will saturate. This will occur when the rate that we create hyperpolarized ^{31}P nuclear spins equals the diffusion rate of that hyperpolarization to the ^{29}Si.

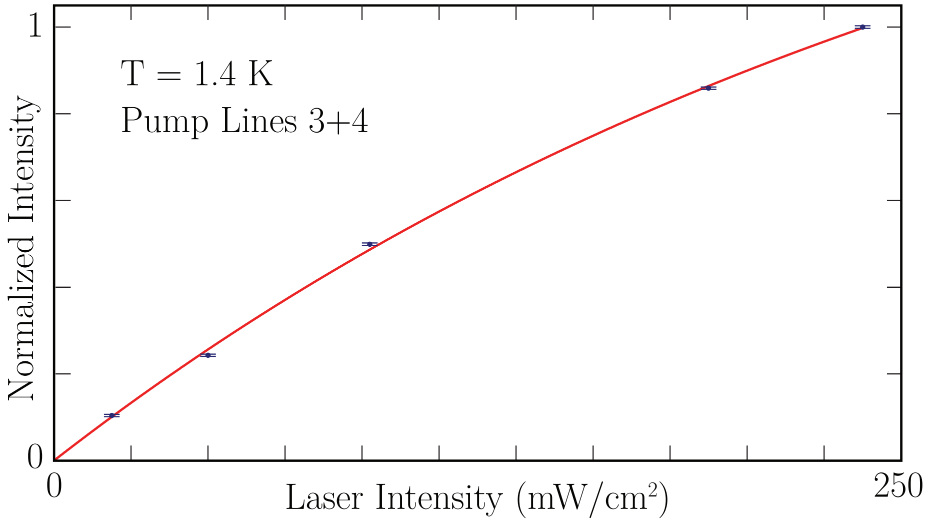

Figure 4.4: This shows the effect varying the laser intensity has on the ^{29}Si polarization when illuminating the sample for 5 minutes at 2.2857 T and 1.4 K. The data is normalized to the maximum value. The data is fit to an exponential that suggests the hyperpolarization rate could be improved at maximum by a factor of ~1.4.

4.3 Total ^{29}Si Hyperpolarization

We have shown that by using the dipole-dipole interaction between ^{31}P and ^{29}Si nuclear spins and choosing a magnetic field that creates a resonance between the nuclear spin systems, we have been able to polarize the ^{29}Si and have demonstrated that this resonant matching condition dramatically improves the spin hyperpolarization transfer to the ^{29}Si. However, ultimately, when looking at how potentially useful this all-optical technique for hyperpolarizing ^{29}Si is, we need to determine how long it takes to hyperpolarize the nuclear spins to a usable degree and determine a value for the polarization. This requires us to look at the dependence of the ^{29}Si polarization on the duration of illumination.

4.3.1 Equilibrium Polarization

Before we can assign absolute ^{29}Si polarization values to the raw data, we must first determine the NMR signal that corresponds to the ^{29}Si polarization when in thermal equilibrium. Since we can easily calculate the ^{29}Si equilibrium polarization (P_0) using Eq. 2.4, the polarization (P) of the ^{29}Si in the resonant coil will be given by $P = \frac{\text{signal}(P)}{\text{signal}(P_0)} P_0$. While the extremely long T_1 of the ^{29}Si makes it ideal for quantum computing and MRI applications, this same property makes it very difficult to measure the thermal NMR polarization signal. This is especially true at the temperatures we have been operating at during this experiment. This became obvious when, after polarizing the ^{29}Si for 30 minutes, we were unable to observe any decay in the signal after 24 hours of hold time in the dark at 4.2 K. Additionally, when starting from an unpolarized state and allowing for $\sim$60 hours of hold time in the dark at 4.2 K, we were unable to see any NMR signal due to the thermal polarization.

However, we recognize that the coupling to the ^{31}P nuclei at the resonant field we are using could provide an effective channel for ^{29}Si nuclear relaxation, but in thermal equilibrium at 4.2 K, there are few ^{31}P nuclei in resonance with the ^{29}Si (the thermal electron polarization is $\sim$0.35 spin-down). At 20 K, the donor electron Boltzmann polarization is only $\sim$0.08 spin-down, the donor $T_{1\mathrm{e}}$ and $T_{1\mathrm{x}}$ are both many orders of magnitude shorter (on the order of microseconds) [59], and the ratio of donor electron spin transition rates $\frac{R_{\downarrow\to\uparrow}}{R_{\uparrow\to\downarrow}} = 0.86$ as opposed to 0.48 at 4.2 K. The net result of having more donors in resonance with the ^{29}Si and operating in a temperature regime such that donor electron spin flips in both directions (from high to low energy and vice versa) are frequent allows for the ^{31}P nuclei to act as an effective ^{29}Si relaxation channel. The experimental data showing the build up of equilibrium polarization at 20 K and 2.2857 T, along with its corresponding exponential fit, is given in Fig. 4.5. From the fit, we extracted the NMR signal that corresponds to the equilibrium polarization and the T_1 relaxation time scale of the ^{29}Si under these conditions. The equilibrium polarization buildup asymptotically approaches $P_0 = 2.31 \times 10^{-5}$ with a corresponding T_1time scale of 33±4 hours. This is in contrast to the ^{29}Si T_1 of $\sim$200 hours at 77 K reported in reference [10] (albeit with a lower ^{31}P doping concentration).

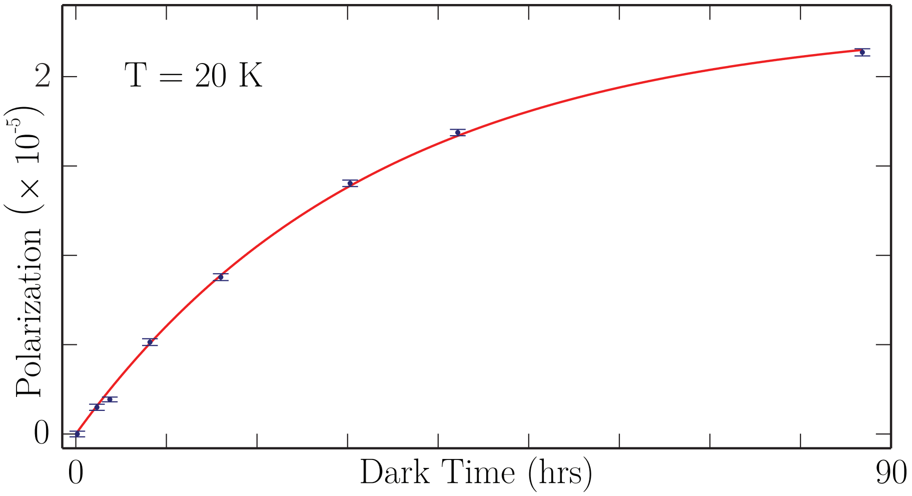

Figure 4.5: This shows the build up of the ^{29}Si thermal equilibrium polarization as a function of hold time in the dark at 20 K and 2.2857 T. The exponential fit returns a ^{29}Si T_1 under these conditions of 33 ± 4 hours.

4.3.2 ^{29}Si Hyperpolarization Build Up

Now that we have determined the NMR signal corresponding to the ^{29}Si equilibrium polarization, we can assign values to its hyperpolarization build up as a function of optical exposure time. Results for this build up of hyperpolarization under maximum optical intensity ($\sim$450 mW $\cdot$ cm^{-2}) with the corresponding exponential fit are shown in Fig. 4.6. After 64 hours of exposure at the ^{31}P-^{29}Si resonant field condition and 1.4 K, we were able to achieve a total hyperpolarization of 6.6±0.4%. The fit returns an asymptotic maximum nuclear hyperpolarization of $13 \pm 2\%$. However, since this value is likely determined by the Overhauser dynamics of the ^{31}P system, we suspect that this limit can be surpassed. Techniques for potentially extending this limiting value and improving the rate of ^{29}Si nuclear hyperpolarization will be discussed in subsequent sections.

4.4 Improving the ^{29}Si Hyperpolarization

Now that we have been able to determine our ^{29}Si polarization values using this all-optical technique, we must look ahead to how we can improve the polarization rate and maximum achievable hyperpolarization. The ways we can improve the hyperpolarization rate can be broken down into two main (though related) areas: considering ways to more effectively transfer hyperpolarization to the ^{29}Si centres; and, increasing the number of hyperpolarized ^{31}P nuclei.

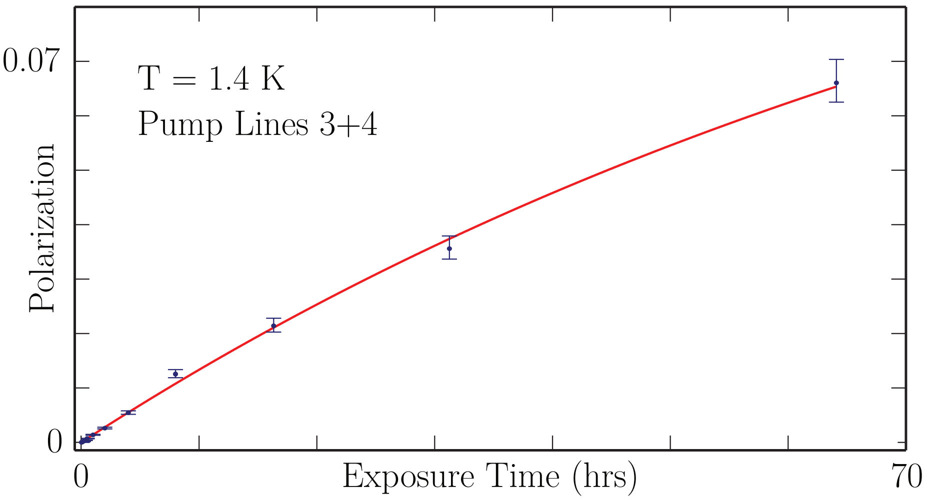

Figure 4.6: This shows the buildup of the ^{29}Si hyperpolarizarization under maximum optical intensity ($\sim$450 mW $\cdot$ cm^{-2}) at 1.4 K and 2.2857 T.

4.4.1 Improving Hyperpolarization Transfer

To more efficiently transfer ^{31}P hyperpolarization to the ^{29}Si we must find ways to have a larger number of ^{31}P experiencing the precise magnetic field that allows for resonant spin diffusion. As discussed in section 4.1.2, the hyperfine interaction between donor electrons and ^{29}Si nuclear spins modifies the ^{31}P-^{29}Si resonance condition and determines the linewidth and asymmetric shape of the resonant transfer peak in Fig. 4.1. The modification of the matching condition for ^{29}Si nuclei located very near the ^{31}P donors is a detrimental effect that reduces the efficiency of nuclear spin flip-flops. This could potentially be mitigated by dithering the applied field over a range determined by the hyperfine-induced linewidth of the resonant transfer peak. This would allow all the ^{29}Si to experience the resonance condition with nearby hyperpolarized ^{31}P. This width is dependent on the impurity concentration of the sample, and though increasing the concentration would increase the number of ^{31}P donors that could transfer hyperpolarization to the ^{29}Si, it would move some of the nuclei out of resonance, especially those near clusters of donors (concentration effects will be considered in more detail in the subsequent section 4.4.2).

4.4.2 Increasing the Number of Hyperpolarized ^{31}P

The simplest way to increase the number of hyperpolarized ^{31}P is by moving to a higher optical intensity. This will improve the donor electron inversion, pushing the electrons further out of equilibrium to drive a stronger NOE while keeping more ^{31}P nuclei in resonance with the ^{29}Si. Another way to increase the number of donor nuclei coupled to the ^{29}Si is by simply increasing the ^{31}P doping concentration. While this will likely improve the ^{29}Si hyperpolarization rate, there is a limit to the improvement that can be provided by increasing the donor concentration. This limit comes as we approach the low temperature Si metal-insulator transition at a ^{31}P doping concentration of $\sim 3-4\times 10^{18}$ cm^{-3} [83]. At concentrations $>10^{-17}$ cm^{-3}, the exchange interaction between donors in clusters of impurities becomes important as the ESR lines broaden [13]. This has a variety of unintended consequences, and may make resonant transfer impossible. For instance, the D^{0}X transitions will broaden as the ^{31}P concentration increases and donor electron exchange interactions become more important. This would force us to dither the laser over a larger range of energies so that the majority of donors are still in optical resonance. Additionally, the donor electron T_{1e} becomes extremely short and we would require higher optical intensity to maintain a high degree of electron population inversion. Most importantly, in this higher doping regime the exchange interaction would broaden the ^{31}P nuclear resonance lines. At the same time, a larger fraction of the ^{29}Si Larmor frequencies will be shifted due to anisotropic hyperfine coupling between donor electrons and ^{29}Si nuclei. This will smear out the ^{29}Si NMR lines and broaden the resonant spin transfer peak seen in Fig. 4.1. This will reduce the rate of spin diffusion from the ^{31}P to ^{29}Si (however, this could be mitigated by dithering B_0 as discussed in sections 4.1.2 and 4.4.1).

Chapter 5

Conclusion and Future Directions

These results demonstrate a method of efficiently hyperpolarizing bulk ^{29}Si spins in silicon doped with phosphorus. This all-optical technique requires no microwave manipulation and uses ^{31}P nuclear spins hyperpolarized by the NOE as the reservoir of polarization. By using the ^{31}P bound exciton transitions to create a negative donor electron spin temperature, we are able to push the donor electron populations much further from equilibrium and drive a stronger NOE than if we had used CW microwave irradiation to saturate the electron spin states. The strong hyperfine interaction between the ^{31}P donor electron and nuclear spins allows the ^{31}P nuclear spins to hyperpolarize much faster than using the coupling between the donor electrons and ^{29}Si spins to hyperpolarize the ^{29}Si nuclei. We chose B_0 to create a switchable, frequency-matched resonance condition between the ^{31}P and ^{29}Si. This allowed the built up ^{31}P hyperpolarization to effectively diffuse out to the nearby ^{29}Si via energy and spin angular momentum conserving flip-flops.

This method for hyperpolarizing ^{29}Si in ^{31}P:Si was able to generate a total hyperpolarization of over 6%, the highest to date for an all-optical hyperpolarization technique. With some improvements (or more patience) it should be possible to push the ^{29}Si hyperpolarization further in the future.

This work is the first to identify this resonance condition between the ^{31}P nuclear spins and ^{29}Si as a switchable coupling that can generate a hyperpolarization. In fact, the matching field condition described here may have contributed to the very high ^{29}Si hyperpolarization ($\sim 10\%$) observed by Dementyev *et al.* in their highly doped ^{31}P:Si sample. These results were taken at 2.35 T, a commonly used field for 100 MHz spectrometers that is coincidentally very near the resonant matching condition we have observed for ^{31}P. This may have contributed to the much stronger DNP signal observed in highly-doped (and hence linewidth-broadened) ^{31}P:Si than that of similarly-doped $^{\text{nat}}$Sb:Si, whose matching field condition lies far away from the magnetic field used in their work.

5.1 Future Directions

While this work has demonstrated an effective and unique way to hyperpolarize ^{29}Si in natural silicon doped with phosphorus, the majority of the measurements we made involved varying the excitation conditions of the laser that hyperpolarized the ^{31}P (e.g. its frequency, intensity, duration), we were not able to experimentally probe all the ways the different factors at work in the system interplayed in a quantitative way. We have demonstrated that resonant transfer from ^{31}P donor nuclei to ^{29}Si is a sizeable effect and that this hyperpolarization technique is effective. If there were to be another series of experiments looking at this process, it would be crucial to devise methods that allow us to determine the time scales of each aspect in this hyperpolarization scheme.

There are three important time scales that each affect the efficiency of this technique. They are the ^{31}P nuclear hyperpolarization time scale, the time scale that governs the diffusion of the ^{31}P nuclear hyperpolarization to the nearby ^{29}Si nuclei, and the bulk ^{29}Si diffusion time scale. Further complicating the interplay of the three time scales is the interaction between donor electrons and the closest ^{29}Si nuclei that alters the resonant matching condition between the two species of nuclei. This is especially true since the probability amplitude of the donor electron wavefunction does not monotonically decrease with distance from the donor [47].

An interesting experiment that could shed some light on the interplay between the ^{31}P hyperpolarization time and the diffusion of that hyperpolarization to the nearby ^{29}Si could be carried out by adding the complexity of pulsed resonant microwave manipulation of the donor electron spin states. Using pulsed resonant microwave manipulation, one could intermix quantum SWAP operations on the ^{31}P donors [84] with the resonant D^0X laser excitation. This would allow the large thermal polarization of the donor electrons at 1.4 K and 2.2857 T to be transferred to the ^{31}P nuclei. Over a period of time t_{wait}, this hyperpolarization would resonantly diffuse to the ^{29}Si. Fig. 5.1 shows how a polarization technique like this could be implemented.

The added complexity in this experiment also has the potential to increase the ^{29}Si hyperpolarization rate in ^{31}P:Si. This scheme would allow us to obtain a very high ^{31}P nuclear polarization on demand and would eliminate the need to rely on the Overhauser dynamics of the system to hyperpolarize the ^{31}P. By relaxing this requirement, the technique could potentially generate a ^{31}P hyperpolarization above the asymptotic value that exists when strictly relying on the NOE. Though there would be many parameters that would need to be considered, adding pulsed resonant microwave manipulation could improve the maximum achievable ^{29}Si hyperpolarization.

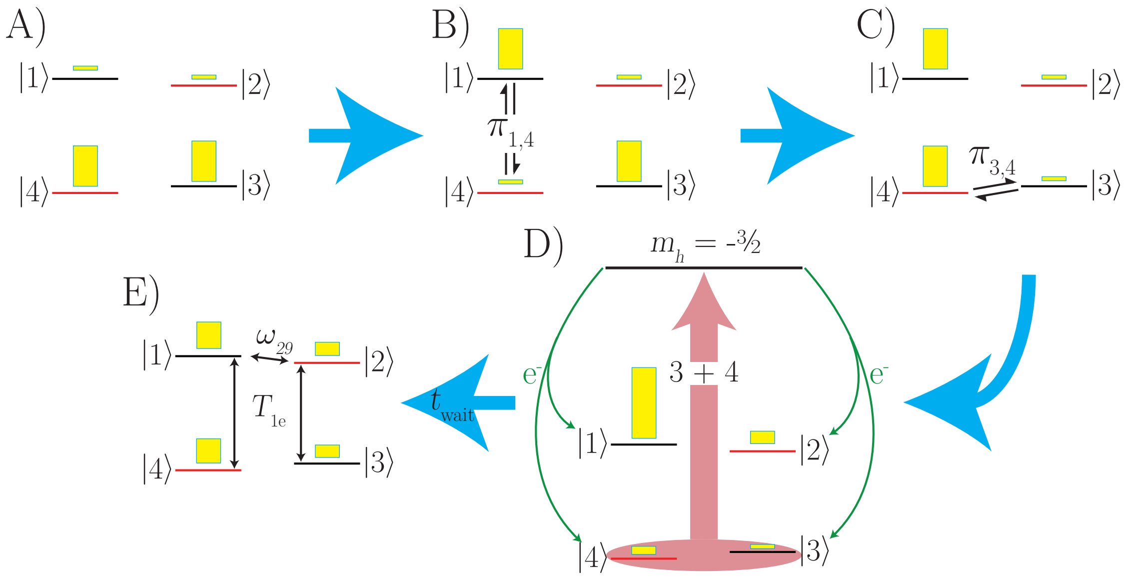

Figure 5.1: An illustration of a ^{29}Si hyperpolarization scheme that uses a quantum SWAP operation to transfer the thermal polarization of the donor electrons to the donor nuclei. A) is the donor thermal polarization before a microwave frequency π pulse exchanges the populations of states $|1\rangle$ and $|4\rangle$ in B). Then in C), a RF π pulse exchanges the populations of $|3\rangle$ and $|4\rangle$. Resonant laser excitation of D^{0}X lines 3 and 4 moves the population from $|4\rangle$ to $|1\rangle$ in D) to generate a strong hyperpolarization in state $|1\rangle$. Then a delay t_{wait} allows the ^{31}P-^{29}Si resonant coupling to facilitate diffusion of the nuclear spin hyperpolarization that has built up in $|1\rangle$ to nearby ^{29}Si in E). During this period, $T_{1\mathrm{e}}$ pushes the donor electrons back towards thermal equilibrium and can allow this procedure to begin again. A significant amount of work would need to be done to optimize all the delays and parameters of this procedure, including t_{wait}.

5.2 Considerations for Applications in Quantum Computation and Magnetic Resonance Imaging

We have identified two primary fields that have the potential to benefit from the technique we developed in this thesis project and the knowledge we have gained about the interaction between ^{31}P and ^{29}Si nuclear spins. As mentioned previously, these are the fields of quantum computing and magnetic resonance imaging. However, since this experiment was performed in a bulk ^{31}P:Si crystal, there are several considerations that need to be taken into account and experiments that need to be performed before the ultimate applicability of this technique into QC and MRI can be assessed.

5.2.1 Quantum Computation

As mentioned in the introduction of this thesis, this ^{29}Si hyerpolarization method would be well suited to initializing the qubits in QC architectures that use linear chains of ^{29}Si embedded in a spin-free ^{28}Si host lattice as qubits [25]. To initialize and readout the ^{29}Si qubits, ^{31}P donors would be placed at the end of the ^{29}Si chains [25]. In the ^{28}Si host crystal that would be used in this implementation, the D^0X lines would be narrow enough to allow the ^{31}P electron and nuclear spin states to be selectively excited. This would allow the ^{31}P electrons and nuclei to be hyperpolarized to $\sim 90\%$ in less than a second. Then, the efficient dipole-dipole coupling between ^{31}P nuclei and ^{29}Si nuclei at the resonant magnetic field used in this work would allow the hyperpolarization to diffuse down the chains of qubits.

This would likely be a very effective method of initializing the qubits in the architecture. Unfortunately, this implementation of QC is currently not one of the frontrunners that the community is considering. Regardless, this work compliments this implementation nicely, and hopefully will add some extra validity to the proposal so its usefulness can be examined in a more practical manner.

5.2.2 Magnetic Resonance Imaging

Using this technique to implement the quantum computing architecture proposed in reference [25] is something that would be far in the future, but the applications of hyperpolarized ^{29}Si as a medical imaging agent seem to be much closer. As mentioned in the introduction, hyperpolarized ^{29}Si in $^{\text{nat}}$Si micro- or nanoparticles can be directly imaged *in vivo* using MRI to aid in diagnosing illnesses in traditionally difficult places to image, like the gastrointestinal tract [17]. First and foremost, before Si micro- and nanoparticles can be used in MRI, more studies of the toxicology of particulate silicon *in vivo* need to be performed. However, the outlook on these technologies achieving widespread use as diagnostic tools is promising [85, 2].

There are a few considerations that would need to be addressed before the ^{29}Si hyperpolarization technique we have developed could be implemented to hyperpolarize the ^{29}Si in Si micro- and nanoparticles. Most importantly, these particles would need to be spectroscopically examined before we could use this technique that employs the ^{31}P D^{0}X transitions as the hyperpolarization mechanism. This is because the bound exciton transitions would need to be fully resolved to use our method. Unfortunately, the crystalline core of these particles are usually surrounded by a layer of amorphous silicon and a layer of silicon dioxide (SiO_2) that will introduce random strain fields due to structural defects on the particle's surface. These strain fields will broaden the D^{0}X lines, and depending on the degree of broadening, make it more difficult or nearly impossible to excite the required D^{0}X transitions in a sufficiently large number of the ^{31}P donors. Due to the small size of the particles, these effects will likely be exaggerated when compared to bulk $^{\mathrm{nat}}$Si.

However, this technique has an advantage over the ones currently employed to hyperpolarize ^{29}Si in silicon micro- and nanoparticles. The current techniques use unpaired electrons associated with dangling bonds on the particle's surface as the reservoir of hyperpolarization and allow the ^{29}Si hyperpolarization to diffuse into the core of the particles [16, 17]. Due to the high density of structural defects, the ^{29}Si in the outer shell or amorphous region of the particle polarizes very quickly. However, it takes a longer time to polarize the silicon in the crystalline core of the particles as the polarized spin system diffuses across the amorphous-crystalline boundary to the core nuclei. These structural defects in the amorphous region are also the primary relaxation channel as the ^{29}Si nuclei return to their equilibrium polarization. To that effect, by considering micro- or nanoparticles with moderate doping levels of donors (10^{15} to 10^{16} cm^{-3}), the method we have developed would be able to hyperpolarize the core ^{29}Si nuclei first. However, to date, researchers have dismissed doped micro- and nanoparticles due to the donor electrons acting as an additional channel for relaxation. Unfortunately, there is a gap in the research in this regard, as there have not been studies looking at the relaxation times of ^{29}Si in moderately doped particles. To date, ^{29}Si relaxation times have only been examined in particles that are nominally undoped and those that are doped to the point where they can almost be considered metals [35]. Experiments in bulk $^{\mathrm{nat}}$Si that measured the ^{29}Si T_1 times as a function of donor concentration have found that T_1 is only weakly dependent on the doping level up to $\sim 10^{16}$ cm^{-3} [67]. This is a gap in the research that ought to be addressed because doping the particles opens up the possibility of employing a number of other ^{29}Si hyperpolarization techniques.

Bibliography

[1] Morton, J. J., McCamey, D. R., Eriksson, M. A. & Lyon, S. A. Embracing the quantum limit in silicon computing. *Nature* **479**, 345–353 (2011).

[2] Atkins, T. M., Cassidy, M. C., Lee, M., Ganguly, S., Marcus, C. M. & Kauzlarich, S. M. Synthesis of long T_1 silicon nanoparticles for hyperpolarized ^{29}Si magnetic resonance imaging. *ACS Nano* **7**, 1609–1617 (2013).

[3] Abragam, A. & Goldman, M. Principles of dynamic nuclear polarisation. *Rep. Prog. Phys.* **41**, 395 (1978).

[4] Crabb, D. & Meyer, W. Solid polarized targets for nuclear and particle physics experiments. *Annual Review of Nuclear and Particle Science* **47**, 67–109 (1997).

[5] Bloembergen, N. Nuclear magnetic relaxation in semiconductors. *Physica* **20**, 1130–1133 (1954).

[6] Bagraev, N. & Zhitnikov, R. Optical orientation of Si^{29} nuclei in n-type silicon and its dependence on the pumping light intensity. *Zh. Eksp. Teor. Fiz* **71**, 952–959 (1976).

[7] Bagraev, N., Vlasenko, L. & Zhitnikov, R. Influence of the depth of location of donor levels on the degree of optical orientation of ^{29}Si nuclei in silicon. *JETP Letters* **24**, 401 (1976).

[8] Vlasenko, L. Excited triplet states of defects and optical nuclear polarization in silicon. *Physica B+C* **116**, 281–286 (1983).

[9] Bagraev, N., Vlasenko, L. & Zhitnikov, R. Inversion of nuclear magnetization of compensated silicon in interband absorption of light in weak magnetic fields. *JETP Letters* **25**, 207–210 (1977).

[10] Lampel, G. Nuclear dynamic polarization by optical electronic saturation and optical pumping in semiconductors. *Phys. Rev. Lett.* **20**, 491–493 (1968).

[11] Bagraev, N. & Vlasenko, L. Optical polarization of nuclei in silicon subjected to optical pumping in weak magnetic fields. *Zh. Eksp. Teor. Fiz* **75**, 1743–1754 (1978).

[12] Bagraev, N. & Vlasenko, L. Optical polarization of lattice nuclei in plastically deformed silicon. *Zh. Eksp. Teor. Fiz.* **83**, 2186–2200 (1982).

[13] Dementyev, A. E., Cory, D. G. & Ramanathan, C. High-field overhauser dynamic nuclear polarization in silicon below the metal–insulator transition. *J. Chem. Phys.* **134**, 154511 (2011).

[14] Hayashi, H., Ko, W., Itahashi, T., Sagara, A., Itoh, K., Vlasenko, L. & Vlasenko, M. Dynamic nuclear polarization of ^{29}Si nuclei in the isotope enriched n-type silicon. *Phys. Status Solidi (C)* **3**, 4388–4391 (2006).

[15] Hayashi, H., Itahashi, T., Itoh, K. M., Vlasenko, L. S. & Vlasenko, M. P. Dynamic nuclear polarization of ^{29}Si nuclei in isotopically controlled phosphorus doped silicon. *Phys. Rev. B* **80**, 045201 (2009).

[16] Dementyev, A. E., Cory, D. G. & Ramanathan, C. Dynamic nuclear polarization in silicon microparticles. *Phys. Rev. Lett.* **100**, 127601 (2008).

[17] Cassidy, M. C., Chan, H. R., Ross, B. D., Bhattacharya, P. K. & Marcus, C. M. *In vivo* magnetic resonance imaging of hyperpolarized silicon particles. *Nat. Nano.* **8**, 363 (2013).

[18] Verhulst, A. S., Rau, I. G., Yamamoto, Y. & Itoh, K. M. Optical pumping of ^{29}Si nuclear spins in bulk silicon at high magnetic field and liquid helium temperature. *Phys. Rev. B* **71**, 235206 (2005).

[19] DiVincenzo, D. P. Quantum computation. *Science* **270**, 255–261 (1995).

[20] Shlimak, I., Safarov, V. & Vagner, I. Isotopically engineered silicon/silicon-germanium nanostructures as basic elements for a nuclear spin quantum computer. *J. Phys.: Condens. Matter* **13**, 6059 (2001).

[21] Ladd, T. D., Goldman, J., Yamaguchi, F., Yamamoto, Y., Abe, E. & Itoh, K. All-silicon quantum computer. *Phys. Rev. Lett.* **89**, 017901 (2002).

[22] Abe, E., Itoh, K., Ladd, T., Goldman, J., Yamaguchi, F. & Yamamoto, Y. Solid-state silicon NMR quantum computer. *J. Supercond. Nov. Magn.* **16**, 175–178 (2003).

[23] Cory, D. G., Laflamme, R., Knill, E., Viola, L., Havel, T., Boulant, N., Boutis, G., Fortunato, E., Lloyd, S., Martinez, R. *et al.* NMR based quantum information processing: Achievements and prospects. *Fortschritte der Physik* **48**, 875–907 (2000).

[24] Vandersypen, L. M., Steffen, M., Breyta, G., Yannoni, C. S., Sherwood, M. H. & Chuang, I. L. Experimental realization of shor's quantum factoring algorithm using nuclear magnetic resonance. *Nature* **414**, 883–887 (2001).

[25] Itoh, K. M. An all-silicon linear chain NMR quantum computer. *Solid State Commun.* **133**, 747–752 (2005).

[26] Ladd, T., Maryenko, D., Yamamoto, Y., Abe, E. & Itoh, K. Coherence time of decoupled nuclear spins in silicon. *Phys. Rev. B* **71**, 014401 (2005).

[27] Vandersypen, L. M. K. & Chuang, I. L. NMR techniques for quantum control and computation. *Rev. Mod. Phys.* **76**, 1037–1069 (2005).

[28] Abe, E., Itoh, K. M., Isoya, J. & Yamasaki, S. Electron-spin phase relaxation of phosphorus donors in nuclear-spin-enriched silicon. *Phys. Rev. B* **70**, 033204 (2004).

[29] Feher, G. Electron spin resonance experiments on donors in silicon. I. electronic structure of donors by the electron nuclear double resonance technique. *Phys. Rev.* **114**, 1219–1244 (1959).

[30] Albert, M., Cates, G., Driehuys, B., Happer, W., Saam, B., Springer, C. & Wishnia, A. Biological magnetic resonance imaging using laser-polarized ^{129}Xe. *Nature* **370**, 199–201 (1994).

[31] Mayo, J. R. & Hayden, M. E. Hyperpolarized Helium-3 Diffusion Imaging of the Lung. *Radiology* **222**, 8–11 (2002).

[32] Day, S. E., Kettunen, M. I., Gallagher, F. A., Hu, D.-E., Lerche, M., Wolber, J., Golman, K., Ardenkjaer-Larsen, J. H. & Brindle, K. M. Detecting tumor response to treatment using hyperpolarized ^{13}C magnetic resonance imaging and spectroscopy. *Nat. Med.* **13**, 1382–1387 (2007).

[33] Shulman, R. G. & Wyluda, B. J. Nuclear magnetic resonance of Si^{29} in n- and p-type silicon. *Phys. Rev.* **103**, 1127–1129 (1956).

[34] Sapoval, B. & Lepine, D. Desaimantation d'un systeme de spins nucleaires dilues relaxation spin-reseau dans le silicium tres pur. *J. Phys. Chem. Solids* **27**, 115–124 (1966).

[35] Aptekar, J. W., Cassidy, M. C., Johnson, A. C., Barton, R. A., Lee, M., Ogier, A. C., Vo, C., Anahtar, M. N., Ren, Y., Bhatia, S. N., Ramanathan, C., Cory, D. G., Hill, A. L., Mair, R. W., Rosen, M. S., Walsworth, R. L. & Marcus, C. M. Silicon nanoparticles as hyperpolarized magnetic resonance imaging agents. *ACS Nano* **3**, 4003–4008 (2009).

[36] Lee, M., Cassidy, M. C., Ramanathan, C. & Marcus, C. M. Decay of nuclear hyperpolarization in silicon microparticles. *Phys. Rev. B* **84**, 035304 (2011).

[37] Hamaguchi, C. & Hamaguchi, C. *Basic semiconductor physics*, vol. 212 (Springer, 2001).

[38] Mohr, P. J., Taylor, B. N. & Newell, D. B. Codata recommended values of the fundamental physical constants: 2010. *Rev. Mod. Phys.* **84**, 1527–1605 (2012).

[39] Cardona, M. & Thewalt, M. L. W. Isotope effects on the optical spectra of semiconductors. *Rev. Mod. Phys.* **77**, 1173–1224 (2005).

[40] Mills, B. Ball-and-stick model of the unit cell of silicon. URL: `http://commons.wikimedia.org/wiki/File:Silicon-unit-cell-3D-balls.png` (2007). File: `Silicon-unit-cell-3D-balls.png`.

[41] Madelung, O., Rössler, U. & Schulz, M. Silicon (Si), indirect energy gap. *Landolt-Börnstein Database - Group III Condensed Matter, Semiconductors, Group IV Elements, IV-IV and III-IV Coumpounds, Part b - Electronic, Transport, Optical and Other Properties* **41A1b** (1989).

[42] Ivey, J. L. & Mieher, R. L. Ground-state wave function for shallow-donor electrons in silicon. II. anisotropic electron-nuclear-double-resonance hyperfine interactions. *Phys. Rev. B* **11**, 849–857 (1975).

[43] Yang, A. *Optical hyperpolarization and detection of electron and nuclear spins of phosphorus donors in highly enriched* ^{28}*Si.* Ph.D. thesis, Department of Physics (2010).

[44] Kohn, W. Shallow impurity states in semiconductors. *Il Nuovo Cimento (1955-1965)* **7**, 713–723 (1958).

[45] Ramdas, A. & Rodriguez, S. Spectroscopy of the solid-state analogues of the hydrogen atom: donors and acceptors in semiconductors. *Rep. Prog. Phys.* **44**, 1297 (1981).

[46] Fletcher, R. C., Yager, W. A., Pearson, G. L., Holden, A. N., Read, W. T. & Merritt, F. R. Spin resonance of donors in silicon. *Phys. Rev.* **94**, 1392–1393 (1954).

[47] Kohn, W. & Luttinger, J. M. Theory of donor states in silicon. *Phys. Rev.* **98**, 915–922 (1955).

[48] Breit, G. & Rabi, I. Measurement of nuclear spin. *Phys. Rev.* **38**, 2082 (1931).

[49] Mohammady, M. H., Morley, G. W., Nazir, A. & Monteiro, T. S. Analysis of quantum coherence in bismuth-doped silicon: A system of strongly coupled spin qubits. *Phys. Rev. B* **85**, 094404 (2012).

[50] Saeedi, K., Simmons, S., Salvail, J. Z., Dluhy, P., Riemann, H., Abrosimov, N. V., Becker, P., Pohl, H.-J., Morton, J. J. & Thewalt, M. L. Room-temperature quantum bit storage exceeding 39 minutes using ionized donors in silicon-28. *Science* **342**, 830–833 (2013).

[51] Schmid, W. Auger lifetimes for excitons bound to neutral donors and acceptors in Si. *Phys. Status Solidi (B)* **84**, 529–540 (1977).

[52] Tajima, M. Determination of boron and phosphorus concentration in silicon by photoluminescence analysis. *Appl. Phys. Let.* **32**, 719–721 (1978).

[53] Yang, A., Steger, M., Karaiskaj, D., Thewalt, M. L. W., Cardona, M., Itoh, K. M., Riemann, H., Abrosimov, N. V., Churbanov, M. F., Gusev, A. V., Bulanov, A. D., Kaliteevskii, A. K., Godisov, O. N., Becker, P., Pohl, H.-J., Ager, J. W. & Haller, E. E. Optical detection and ionization of donors in specific electronic and nuclear spin states. *Phys. Rev. Lett.* **97**, 227401 (2006).

[54] Thewalt, M., Yang, A., Steger, M., Karaiskaj, D., Cardona, M., Riemann, H., Abrosimov, N., Gusev, A., Bulanov, A., Kovalev, I., Kaliteevskii, A., Godisov, O., Becker, P., Pohl, H., Haller, E., Ager III, J. & Itoh, K. Direct observation of the donor nuclear spin in a near-gap bound exciton transition: ^{31}P in highly enriched ^{28}Si. *J. of Appl. Phys.* **101**, 081724 (2007).

[55] Feher, G. & Gere, E. A. Electron spin resonance experiments on donors in silicon. II. electron spin relaxation effects. *Phys. Rev.* **114**, 1245–1256 (1959).

[56] Song, Y. & Dery, H. Analysis of phonon-induced spin relaxation processes in silicon. *Phys. Rev. B* **86**, 085201 (2012).

[57] Honig, A. & Stupp, E. Electron spin-lattice relaxation in phosphorus-doped silicon. *Phys. Rev.* **117**, 69–83 (1960).

[58] Wilson, D. K. & Feher, G. Electron spin resonance experiments on donors in silicon. III. investigation of excited states by the application of uniaxial stress and their importance in relaxation processes. *Phys. Rev.* **124**, 1068–1083 (1961).

[59] Castner, T. G. Raman spin-lattice relaxation of shallow donors in silicon. *Phys. Rev.* **130**, 58–75 (1963).

[60] Tyryshkin, A. M., Lyon, S. A., Astashkin, A. V. & Raitsimring, A. M. Electron spin relaxation times of phosphorus donors in silicon. *Phys. Rev. B* **68**, 193207 (2003).

[61] Hill, T. L. *An introduction to statistical thermodynamics* (Courier Dover Publications, 2012).

[62] Overhauser, A. W. Polarization of nuclei in metals. *Phys. Rev.* **92**, 411 (1953).

[63] Carver, T. R. & Slichter, C. P. Experimental verification of the overhauser nuclear polarization effect. *Phys. Rev.* **102**, 975–980 (1956).

[64] McCamey, D. R., van Tol, J., Morley, G. W. & Boehme, C. Fast nuclear spin hyperpolarization of phosphorus in silicon. *Phys. Rev. Lett.* **102**, 027601 (2009).

[65] Abragam, A. & Hebel, L. The principles of nuclear magnetism. *American Journal of Physics* **29**, 860–861 (1961).

[66] Hale, E. B. & Mieher, R. L. Shallow donor electrons in silicon. I. hyperfine interactions from endor measurements. *Phys. Rev.* **184**, 739–750 (1969).

[67] Lampel, G. & Solomon, I. Physique des solides-determination de la densite des electrons de conduction a lemplacement des noyaux dans le silicium peu dope. *Comptes Rendus Hebdomadaires des Seances de l'Academie des Sciences* **258**, 2289 (1964).

[68] Saykin, S., Mozyrsky, D. & Privman, V. Relaxation of shallow donor electron spin due to interaction with nuclear spin bath. *Nano Letters* **2**, 651–655 (2002).

[69] Solomon, I. Relaxation processes in a system of two spins. *Phys. Rev.* **99**, 559–565 (1955).

[70] Khutsishvili, G. Spin diffusion. *Sov. Phys. Usp.* **8**, 743–769 (1966).

[71] Hayashi, H., Itoh, K. M. & Vlasenko, L. S. Nuclear magnetic resonance linewidth and spin diffusion in ^{29}Si isotopically controlled silicon. *Phys. Rev. B* **78**, 153201 (2008).

[72] Fukushima, E. & Roeder, S. B. *Experimental pulse NMR: a nuts and bolts approach* (Addison-Wesley Reading, MA:, 1981).

[73] Yang, A., Steger, M., Sekiguchi, T., Thewalt, M., Ladd, T., Itoh, K., Riemann, H., Abrosimov, N., Becker, P. & Pohl, H.-J. Simultaneous subsecond hyperpolarization of the nuclear and electron spins of phosphorus in silicon by optical pumping of exciton transitions. *Phys. Rev. Lett.* **102**, 257401 (2009).

[74] Janis Research Company, 2 Jewel Drive, P.O. Box 696, Willmington, MA 01887, USA. *Operating Instructions for Superconducting Magnet Systems.*

[75] Koheras, Blokken 84, DK-3460 Birkerød, Denmark. *Koheras Adjustik System Manual*, 1.0 edn. (2006).

[76] SpinCore Technologies, Incorporated, 4631 NW 53rd Avenue, Suite 103, Gainesville, FL 32653, USA. *RadioProcessor Manual* (2008).

[77] Traficante, D. D. Introduction to transmission lines basic principles and applications of quarter-wavelength cables and impedance matching. *Concepts in Magnetic Resonance* **5**, 57–86 (1993).

[78] Vlasenko, L., Martynov, Y. V., Gregorkiewicz, T. & Ammerlaan, C. Electron paramagnetic resonance versus spin-dependent recombination: Excited triplet states of structural defects in irradiated silicon. *Phys. Rev. B* **52**, 1144 (1995).

[79] Saikin, S. & Fedichkin, L. Nonideality of quantum operations with the electron spin of a ^{31}P donor in a si crystal due to interaction with a nuclear spin system. *Phys. Rev. B* **67**, 161302 (2003).

[80] Ramanathan, C. Dynamic nuclear polarization and spin diffusion in nonconducting solids. *Applied Magnetic Resonance* **34**, 409–421 (2008).

[81] Feher, G. Nuclear polarization via "hot" conduction electrons. *Phys. Rev. Lett.* **3**, 135–137 (1959).

[82] Yosida, K. Magnetic properties of Cu-Mn alloys. *Phys. Rev.* **106**, 893–898 (1957).

[83] Ochiai, Y. & Matsuura, E. Metal-semiconductor transition in heavily doped n-type silicon. *Phys. Status Solidi (A)* **27**, K89–K91 (1975).

[84] Simmons, S., Brown, R. M., Riemann, H., Abrosimov, N. V., Becker, P., Pohl, H.-J., Thewalt, M. L. W., Itoh, K. M. & L., M. J. J. Entanglement in a solid-state spin ensemble. *Nature* **470**, 69 (2011).

[85] Godin, B., Gu, J., Serda, R. E., Bhavane, R., Tasciotti, E., Chiappini, C., Liu, X., Tanaka, T., Decuzzi, P. & Ferrari, M. Tailoring the degradation kinetics of mesoporous silicon structures through pegylation. *J. Biomed. Mater. Res. A* **94**, 1236–1243 (2010).